Experimental Investigation of Coandă Flow Attachment in Automotive Windshield Defrosting

Alexander Schukmann[1,2*], Timo Gericke[1] and Andrea Beck[2]

[1]Volkswagen AG, Wolfsburg, Germany.
[2]Institute of Aerodynamics and Gas Dynamics, University of Stuttgart, Stuttgart, Germany.

*Corresponding author. E-mail: alexander.schukmann@volkswagen.de;
Contributing authors: timo.gericke@volkswagen.de; andrea.beck@iag.uni-stuttgart.de;

Abstract

This paper examines the occurrence of the Coandă-effect in the context of automotive windshield defrosting. A generic, parameterized pseudo-2D test rig representing the main windshield-defrosting components of a passenger vehicle, is introduced. By externally controlling key geometric features such as the defrost duct angle and dashboard position, attachment of the defrost jet to the dashboard due to the Coandă effect is induced, which is incompatible with the functional requirements of passenger-vehicle HVAC systems. By exploiting the tendency of Coandă flows to exhibit hysteresis, steady mono- and bistable states are identified in which the turbulent defrost jet remains attached either to the windshield or the dashboard over extended time periods, as well as unsteady configurations characterized by random switching between states. Two-dimensional two-component particle image velocimetry (2D2C PIV) is used to analyze the mean flow fields of the identified jet states in terms of velocity and turbulent kinetic energy contours, maximum velocity decay, and half-width growth rates. In addition, pressure coefficients measured along the windshield centerline demonstrate how proximity to the dashboard alters the pressure distribution to resemble that of a shallower duct angle through deflection of the defrost jet. Proper orthogonal decomposition is applied to the PIV data to extract the switching modes and their associated temporal coefficients, with subsequent statistical analysis indicating that the observed state switching exhibits Poissonian characteristics. Beyond the present study, the experimental data are intended to serve as a benchmark for the validation and assessment of CFD results.

Keywords: Automotive windshield defrosting, Coandă effect, flow bistability, oblique jet impingement, oblique wall-attaching jet, particle image velocimetry

1 Introduction

Warm, humid air from inside the cabin of passenger vehicles can condense on the colder windshield and/or form a layer of frost during the cold winter months, significantly impairing the visibility of the driver. Fast and reliable defrosting and demisting of the vehicle windshield by the heating, ventilation and air-conditioning unit (abbr. HVAC) therefore represents an important safety-related requirement and is subject to clear legal regulations. Individual components of the HVAC system are shown in Fig. 1a. Heated dry air from the blowing unit passes through the air inlet and exits the defroster grille to be directed by the guiding vanes towards the windshield. An ideal defrosting/demisting pattern is schematically depicted in Fig. 1b. The jet from the primary defrost duct impinges on the windshield at approximately one-third of the windshield length measured from its base and ensures continuous clearing up to the header, with a slight preference for the driver's side area (I), which has to be ice-/mist-free to 80% within 20 minutes [1]. The complete viewing area (II) must be cleared to 90% within 40 minutes. A secondary duct located at the windshield base ensures coverage of the lower windshield area. To satisfy these conditions and ensure adequate visibility for the driver, it is crucial that the airstream from the defroster duct remains stably attached to the inner surface of the windshield. However, it can be observed that the airflow may detach from the windshield either partially or across its entire width and instead adhere to the dashboard, due to the so-called Coandă effect, which describes the tendency of a fluid jet to attach to flat or curved surfaces.

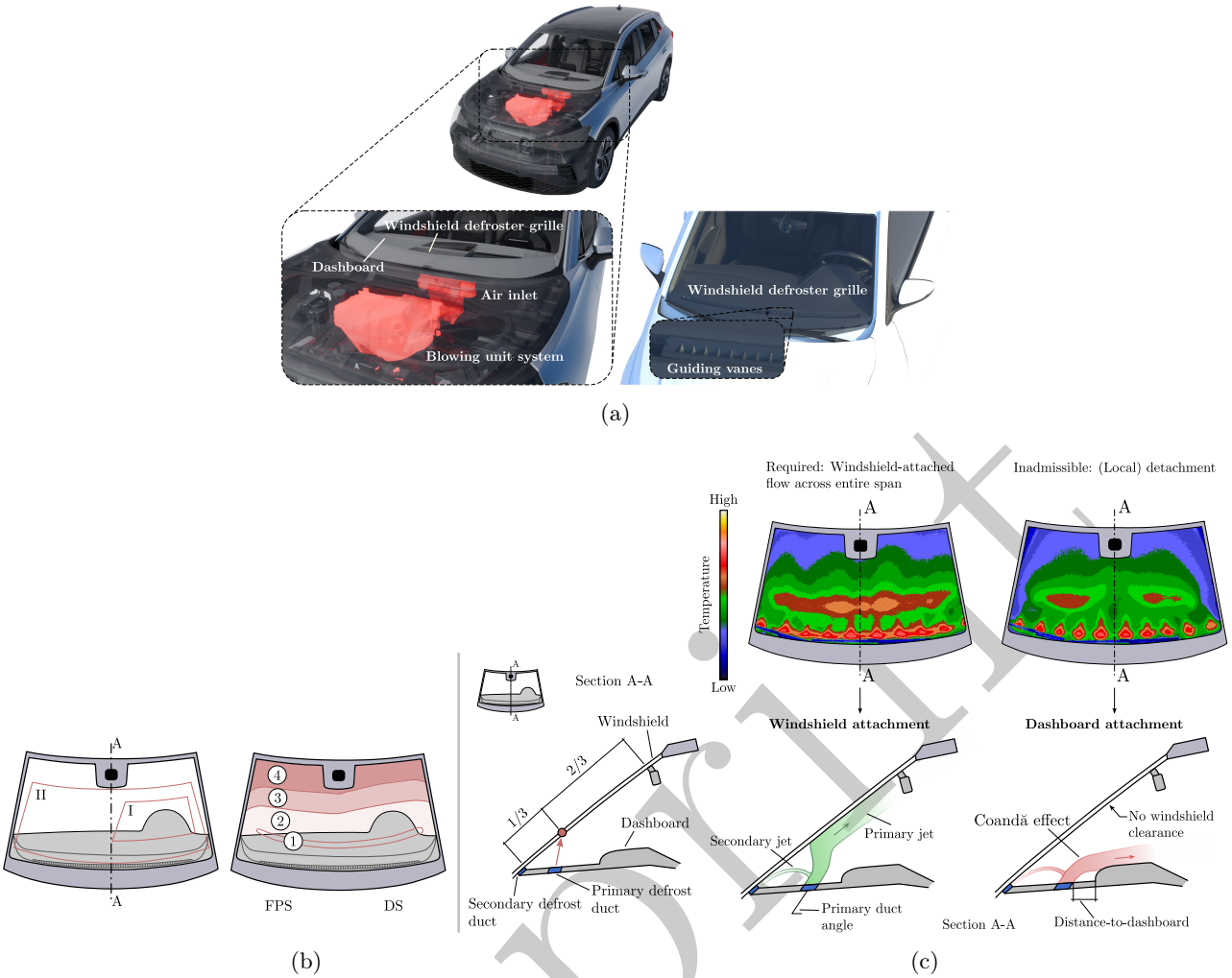

Fig. 1: **(a)** HVAC system components in a Volkswagen ID.4 (left) and Volkswagen Polo 2018 TSI. **(b)** Schematic depiction of windshield defrosting/demisting area and impact region of the primary defrosting jet. FPS: Front passenger side, DS: Driver side. **(c)** Top: Infrared-Thermogram showing the detachment from the interior surface of the windshield due to the Coandă effect and the associated attachment to the dashboard. Bottom: Illustration of windshield- and dashboard-attached flow.

The Coandă effect appears to have been first described by Thomas Young in 1800 [2, 3] and was later named by von Kármán after Romanian engineer Henri Coandă, who applied it in a number of patents for aviation technology [4, 5]. Since then, it has been utilized in a variety of engineering applications, ranging from fluidic oscillators [6], drag reduction for ships [7], fluidic thrust vectoring control [8] and attitude control in internal combustion engines [9], to improving energy efficiency in building ventilation [10]. In some cases, its occurrence is undesirable and can lead to intricate and challenging-to-control flow conditions, especially when potential adherence to multiple surfaces and geometric complexity are involved, such as in intracardiac blood flow [11], space launch systems [12], uncontrolled deflection in jet vectoring [13] or annular swirling [14] and impinging jets [15]. In the instances listed, multimodal behavior is reported due to the tendency of Coandă flows to exhibit hysteresis, that is, multiple flow solutions can exist under identical conditions depending on the previously adopted state. Dynamic behavior in the form of stochastic perturbation-induced state-switching may emerge as a consequence [16, 17].

The hysteretic character of Coandă flows was first described by Newman [18] and Bourque and Newman [19] in 1960, who studied this effect for an oblique wall-attaching jet. Depending on whether the angle of inclination of the plate was increased starting from an attached jet or decreased starting from a free jet, it was possible to observe both states within a certain angle interval, as a function of the plate-length-to-slot-width ratio. Later, similar experiments have been conducted by Allery et al. [20] and more recently by Skotnicka-Siepsiak [21], who both found an increase of the hysteresis interval with the Reynolds number. However, the predicted relationships between the Reynolds number and the critical interval angles themselves is contradictory, as is noticed in the latter study and therefore remains an open question.

Within the context of automotive windshield defrosting, the appearance of the Coandă effect is demonstrated in Fig. 1c on the right by means of an infrared thermogram, which illustrates the temperature distribution

on the interior side of the windshield. Around the central and peripheral area of the windshield, a significant temperature decrease can be identified where heat transfer from the defrost jet to the windshield is insufficient, resulting in reduced or even absent defrosting coverage. This pattern arises from the Coandă effect, which in this particular case causes the jet to detach locally from the inner windshield surface. A design exhibiting this behavior is unacceptable; early identification during the development process is therefore essential to prevent costly revisions and to ensure reliable system performance. Nevertheless, to the best of the authors' knowledge, a systematic investigation of the factors governing the occurrence of the Coandă effect in the context of windshield defrosting is still missing.

Available studies on windshield defrosting/demisting through the HVAC unit generally cover the thermofluid dynamics of the defrost airstream impinging on the windshield to analyze and optimize its defrosting pattern, heat-transfer characteristics and spatial redistribution within the cabin to maximize passenger comfort [22–32]. Early studies include research by Sakamoto et al. [33], who used helium bubble tracing to improve the air distribution on the vehicle windows and within the compartment of a simplified car model by variation of the defrosting duct angle (cf. Fig. 1c) and its distance to the windshield. Ikeda et al. [34] and Sugano et al. [35] applied CFD techniques to calculate the three-dimensional flow field and achieved good agreement with experiments.

AbdulNour [36] carried out hot-wire anemometry in the vicinity of the defrost duct outlet and the interior side of the windshield and used this data for validation of CFD simulations of the three-dimensional defroster flow of a model vehicle [37, 38].

Skea et al. [39] compared clearing patterns on a real vehicle windshield between finite volume and lattice Boltzmann CFD methods with thermal imaging and obtained satisfactory results.

Becker et al. [40] performed laser-Doppler anemometry (abbr. LDA) to analyze the defroster flow field in a real automobile. In the same study, they conducted LDA and thermal imaging measurements on an oblique-plate impinging slot jet under isothermal and heated conditions, serving as a simplified model of a car defroster geometry. By estimating the local Richardson number in the non-isothermal case and direct comparison of the LDA results with those of the unheated jet, it was determined that buoyancy effects on the flow field are negligible under realistic circumstances. In a similar setup, Roy et al. [41] used CFD to calculate the three-dimensional flow field created by jets from two adjacent slots impinging on an inclined flat plate. They validated the predicted local heat transfer coefficients on the plate surface through experiments.

A common limitation among the cited studies is the absence of any substantial dashboard geometry in their vehicle models: the instrument panel is often aligned flush with the nozzle outlet or not included at all. Furthermore, the defrost duct has a steep angle that is clearly directed towards the windshield. Indications of a detrimental influence of the dashboard on the defrosting performance can be found, for example, in the study by Kang et al. [42], who recommend minimizing the dashboard height extending above the duct exit and maintaining a ratio between the distance-to-dashboard (cf. Fig. 1c) and the height greater than unity.

Nasr et al. [43] and Patidar [44] emphasize the need to avoid separation from the windshield in the design of defrost systems, while Sen et al. [45] explicitly mention avoiding the Coandă effect.

Further notable references include an article from 2007 written by Kogler et al. [46] for the magazine ATZ worldwide describing optimization of the outflow angle in their indirect ventilation concept using numerical simulation to avoid attachment of the flow to the dashboard.

Despite not being explicitly stated, the streamline distribution of the defrost jet in a CFD study conducted by Yang et al. [47] indicates partial attachment to the dashboard that has been improved by adjustment of the guiding vanes.

A comprehensive study comparing experimental, numerical and theoretical approaches for the analysis of a jet exiting a simplified automotive cabin vent model has been conducted recently by Sip et al. [48], including attachment of the jet to a neighboring wall that was meant to mimic proximity to the side windows and doors in a car cabin.

This survey supports the authors' belief that the occurrence of the Coandă effect in the context of automotive windshield defrosting has not yet been satisfactorily addressed in the existing literature.

At this point, it is worth mentioning the broader research field of wall-attaching and impinging jet flows outside of the context of windshield defrosting. The term oblique wall-attaching offset jet (OWAOJ) generally refers to a jet issuing from a nozzle located at an offset from a wall that is tilted away from the jet. In contrast, for an oblique-plate impinging jet (OPIJ) the plate is tilted toward the jet, such that the virtual extension of the nozzle axis intersects the plate downstream of the nozzle. A survey on experimental and numerical studies regarding (O)WAOJ can be found in [49] and a comprehensive review on (O)PIJ is given in [50]. Following this classification, the windshield-attached defrost jet is akin to an OPIJ, whereas dashboard-attached flow falls into the category of OWAOJ. Despite similarities to these canonical jet flows, the defrost system exhibits several distinctive features that motivate the need for more specific test cases. These include the location and geometry of the dashboard, which are expected to significantly affect the qualitative and quantitative characteristics of the flow field even without occurrence of the Coandă effect, as well as the interaction between the primary and

secondary jets (cf. 1c). Furthermore, the presence of guiding vanes in automotive defrosting vents affects key properties of the flow field, such as the centerline velocity decay and jet direction [48].

In this paper, we present an experimental study based on a generic parameterized pseudo-2D test rig for the identification of bistable jet states under flow conditions akin to those in real vehicle windshield defrosting/demisting. Since the focus here is on the fluid-dynamic properties associated with the Coandă effect, an isothermal setup with an unheated jet is used. The geometry of this test rig previously served as the basis for a numerical study carried out by Müller et al. [51], which revealed that both windshield- and dashboard-attached flow states can constitute attractors of the numerical model for a given set of parameters. In addition, the analysis hinted at a decisive impact of the flow conditions within the defrost duct on the observed bifurcation.

In view of all aforementioned considerations, the investigations described in this paper fulfill the following purposes:

- Verify whether bistable flow behavior can be observed in the context of vehicle windshield defrosting.
- Improve the understanding of the flow physics in various states of the defrost jet.
- Identify the influence of several key factors on the occurrence and extent of the Coandă effect.
- Provide comprehensive experimental validation data for numerical simulations based on a simplified, precisely known geometry, including the inflow conditions, as these have a decisive influence on physical modeling in CFD.

The flow field is analyzed using two-dimensional two-component particle image velocimetry measurements (abbr. 2D2C PIV) in the mid-plane of the test rig. Additional pressure measurements along the windshield centerline are used to characterize the pressure distribution for windshield-attached flow. The dashboard position and duct angle are externally controlled using a linear stage and collaborative robot, respectively, allowing modification of the specified parameters without disturbing the flow field.

Using this setup, attachment of the defrost jet to the dashboard due to the Coandă effect is triggered in a reproducible fashion. Depending on the parameter values, the jet exhibits several distinct steady and unsteady flow configurations. In addition to regions of monostable behavior, in which the jet attaches exclusively to either the windshield or the dashboard, parameter ranges exist in which both attachment states remain stable over extended periods of time due to hysteresis associated with the Coandă effect. These states are characterized in terms of the pressure distribution along the windshield, centerline velocity decay and growth rates. Proper orthogonal decomposition (POD) is applied to extract temporal coefficients of the switching modes in unsteady operating points. Subsequent statistical analysis reveals the random nature of the observed state switching.

The remainder of the paper is organized as follows. Section 2 describes the experimental setup and introduces the relevant terminology. Section 3 presents and discusses the results, including the identification of mono- and bistable configurations and a detailed characterization of the corresponding flow fields. Finally, section 4 concludes the study.

2 Experimental Setup

2.1 Defrost Test Rig and Flow Configuration

The principal components of the pseudo-2D defrost test rig are displayed in Fig. 2. Its main body consists of a $\mathrm{L} \times \mathrm{W} \times \mathrm{H} = 838 \times 1038 \times 920\,\mathrm{mm}^3$ wooden plenum, which is fed by the primary air supply fan via a $\varnothing 100\,\mathrm{mm}$ pipe inserted into its front side. The air first enters a cavity that is closed off at the top by a cover plate, before passing through a perforated metal sheet into the 100 mm wide vertical inflow section of the primary defrost duct. The latter is formed by two aluminum plates whose inclination angle can be adjusted by means of a rotating mechanism consisting of a connecting rod and rotary disk. This rotary disk is connected through a custom-made adapter to the last wrist joint of a six-axis collaborative robot (cobot) model UR5 from Universal Robots with a pose repeatability of $\pm 0.1\,\mathrm{mm}$. The pivot point of the two plates that form the duct walls is located at their upper edge, where they are fixed to the horizontally mounted upper cover plate of the main plenum. Their shape creates a physical stop that determines the limit positions of rotation. During the experiments, the angular position of the rotary disk connected to the cobot is externally controlled via RoboDK software and converted to the corresponding value of the primary duct angle. The procedure for this conversion is described in detail in suppl. Sec. 1.2 and 1.3 of the supplemental material.

Bridges installed on the lateral ends of the primary duct connect the two parts of the cover plate separated by the duct, whereby one of these bridges is made of acrylic glass to ensure visual accessibility of the PIV cameras (cf. Sec. 2.2) to the interior of the duct.

The main plenum is supported by an aluminum-profile frame, into which a secondary frame enclosing the acrylic-glass windshield is mounted in a rotatable support and laterally secured via clamp bolts. An additional wooden enclosure is fastened to the lower section of the secondary frame, forming the inflow plenum for the secondary defrost jet. This jet, which is present in actual vehicle defroster systems to clear the lower region of the windshield not fully accessible to the primary jet, is included in the model setup to establish realistic

conditions. Similar to the primary inflow, its mass flow rate can be set independently via a fan that is controlled through a laboratory power supply. The air exits the secondary defrost duct after passing through another perforated plate inside the secondary plenum.

A geometrically simplified, interchangeable dashboard dummy is mounted on top of the cover plate, with its distance from the discharge of the primary defrost duct adjustable via a linear translation stage (model OptoSigma Micro Stage 26-100). In real cars, the protruding geometry of the dashboard serves as a visual barrier that hides the slot exit from the passengers line of sight. Without it, no attachment of the jet onto the top panel occurred in our setup. The Micro Stage offers a total travel range of 100 mm with a positioning accuracy of 10 µm.

To promote two-dimensionality of the flow field, the test rig is designed to achieve duct-width-to-spanwise-length aspect ratios (AR), which exceed general thresholds found in the literature, see Table 2 (according to Pope [52], a typical value is AR > 50, Deo et al. [53] report at least AR > 20 for plane jets to exhibit statistically two-dimensional properties of the mean velocity field). Furthermore, glass side walls are installed to extend the region of two-dimensionality by suppressing lateral entrainment of air [54] and simultaneously ensure visible access. Any gaps between the side walls and the upper cover plate as well as the secondary frame are sealed using pressure pads distributed along the edges of the glass window, with self-adhesive felt strips in between.

To minimize surface reflections during PIV investigations, the surfaces exposed to the laser sheet are covered with self-adhesive matte black film from d-c-fix. This includes the interior of the primary and secondary defrost ducts as well as the top side of the test rig, along with the dashboard dummy.

To enable experimental determination of the inflow conditions using PIV, acrylic glass windows are installed at suitable locations in both plena. Furthermore, the main compartment has three window inserts to evaluate the air distribution in the inflow area of the primary defrost channel along the spanwise direction. In addition, pressure taps and thermocouples are installed in both inflow sections to facilitate the specification of suitable boundary conditions for numerical simulations in the future. Their locations, the positions and sizes of the window inserts as well as other test rig dimensions, can be taken from supp. Fig. 7.

The test rig is parameterized and partially modulary structured, allowing various configurations to be implemented with comparatively minor effort. An overview of the modifiable parameters is given in Fig. 3a, whereby the geometrical parameters varied primarily during the investigation presented in Sec. 3 are highlighted in red and include the primary duct angle β and the distance from the duct exit to the dashboard L_s. The simplified dashboard geometry used in this study consists of a wooden board with a quarter-cylindrical front part (cf. Fig. 3b). All parameter values were selected to closely represent conditions in a real passenger car and are summarized in Table 1.

As the axis of rotation of the primary defrost duct walls is located at their respective upper edges, the effective cross-sectional duct area A_{eff} changes with the inclination angle of the duct β. Since the associated effective duct width $L_{d,\mathrm{eff}} = L_d \sin\beta$ and the nominal jet exit velocity $U_{\mathrm{j}} = \dot{m}_{1,\mathrm{N}}/\rho_{\mathrm{air}} A_{\mathrm{eff}}$ are used for nondimensionalization in Sec. 3, an overview of these and other parameters affected by a variation in β for the three main angles investigated is summarized in Table 2.

Table 1: Overview of test rig parameters. Values in parentheses correspond to additional investigations concerning the qualitative influence of the respective parameter.

Windshield angle (measured against horizontal)	α	35°
Primary duct angle (measured against horizontal)	β	45.0°–84.9°
Primary duct-to-dashboard distance	L_s	0 mm–100 mm
Windshield-to-primary duct distance	L_b	67 mm
Primary duct exit width	L_d	13.9 mm
Primary duct length	L_1, L_2	43 mm
Secondary duct width	L_r	6 mm
Windshield length (base to tip)	L_w	866 mm
Primary duct inflow section width	L_a	100 mm
Dashboard geometry	G_s	cylindrical
Spanwise extent of the test section	L_z	1000 mm
Nominal primary duct mass flow rate	$\dot{m}_{1,\mathrm{N}}$	180 kg h^{-1}
Nominal secondary duct mass flow rate	$\dot{m}_{2,\mathrm{N}}$	18 kg h^{-1}

2.2 Measurement Techniques

Non-time-resolved 2D2C particle image velocimetry investigations were conducted in the central plane of the pseudo-2D defrost test rig to analyze the flow field for various parameter configurations described in Sec. 2.1 and identify mono- and bistable states. The LaVision system consisted of a double-pulsed Nd:YAG laser with a

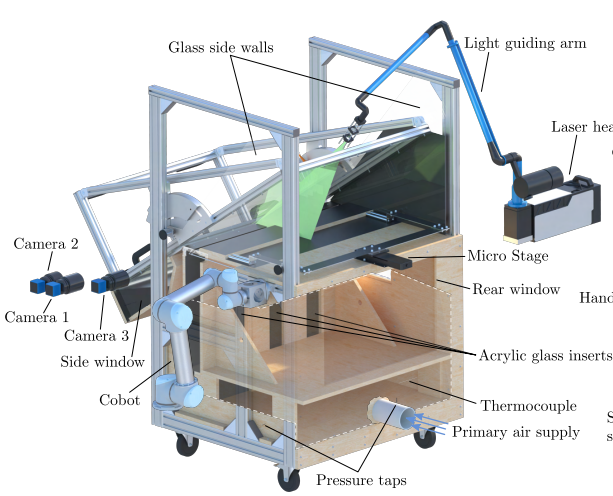

(a) Front side view.

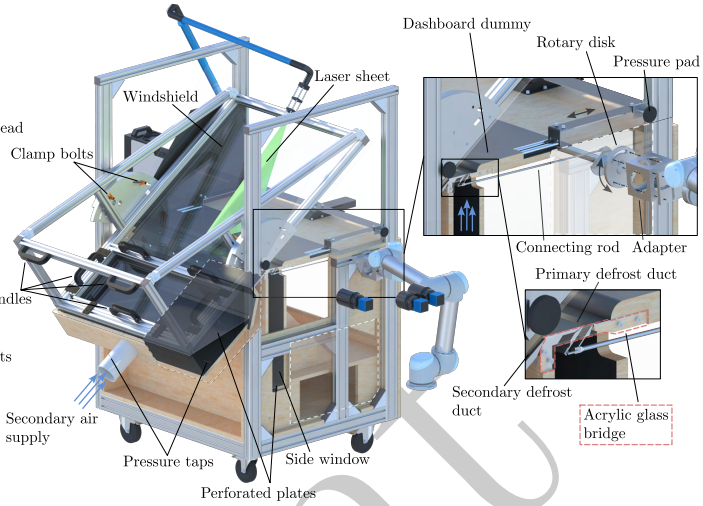

(b) Rear side view.

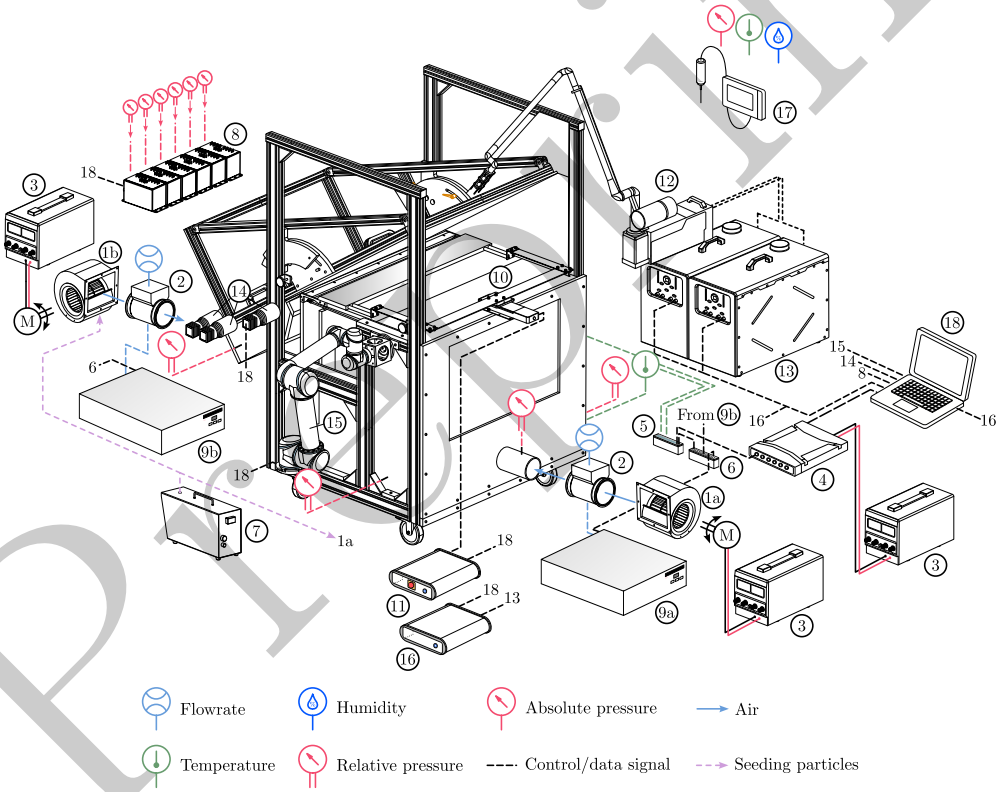

① : Air supply fan
② : Thermal mass flowmeter (ABB Sensyflow P)
③ : Laboratory power supply (EA-PS 2016-100)
④ : Electronic control unit (ETAS ES892.1)
⑤ : Thermo module (CSM Thermo-Scan MiniModul 16 Pro)
⑥ : Analog-to-digital converter (CSM AD-Scan MiniModul Pro)
⑦ : Seeding device (TSI Portable Test Aerosol Generator Model 3073)
⑧ : Pressure scanner (Scanivalve DSA 3217/16Px)
⑨ : Sensyflow P supply/evaluation unit
⑩ : Translation stage (OptoSigma Micro Stage 26-100)
⑪ : LaVision Micro Stage Controller
⑫ : Laser head (Quantel EverGreen HP)
⑬ : EverGreen HP power supply
⑭ : PIV camera (LaVision Imager CX12)
⑮ : Collaborative robot (Universal Robots UR5)
⑯ : LaVision Programmable Timing Unit X
⑰ : Humidity and temperature probe (Vaisala HMP1)
⑱ : Computer

(c) Overview of the experimental setup

Fig. 2: Pseudo-2D defrost testrig.

Table 2: Jet configurations with changing primary duct angle.

Description	Parameter	$\beta = 45.0°$	$\beta = 61.9°$	$\beta = 80.6°$
Effective primary duct width in mm	$L_{d,\mathrm{eff}}$	9.8	12.3	13.7
Nominal jet exit velocity in $\mathrm{m\,s^{-1}}$	U_j	4.2	3.4	3.0
Windshield-spacing-to-duct-width ratio	$H/L_{d,\mathrm{eff}}$	≈ 28	≈ 9	≈ 5
Offset-to-duct-width ratio	$L_b/L_{d,\mathrm{eff}}$	≈ 6.8	≈ 5.5	≈ 4.9
Primary duct aspect ratio	$L_z/L_{d,\mathrm{eff}}$	≈ 102	≈ 82	≈ 73
Reynolds number	$\mathrm{Re} = U_\mathrm{j} L_{d,\mathrm{eff}}/\nu_\mathrm{air}$	2800	2800	2800

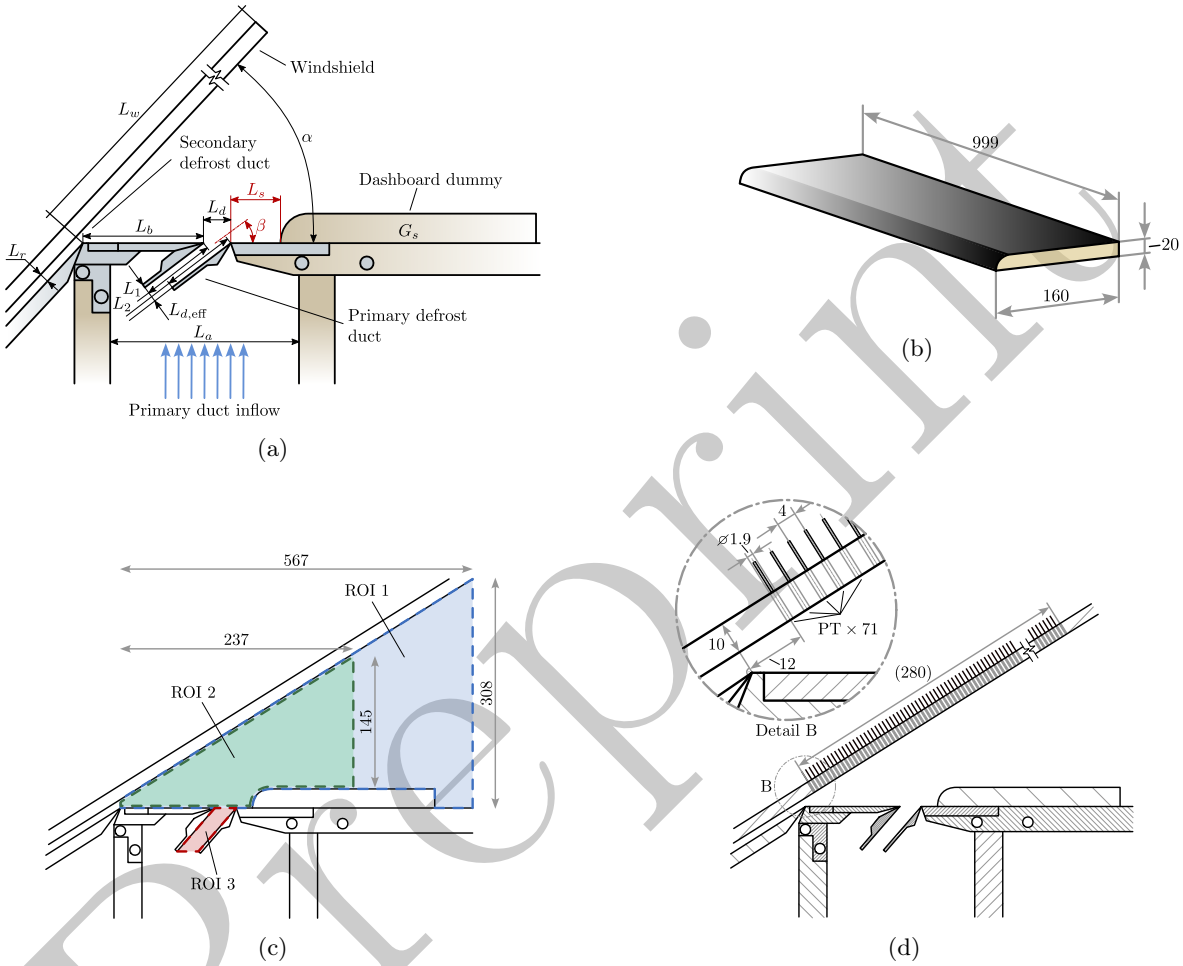

Fig. 3: **(a)** Overview of test rig parameters. Parameters highlighted in red are varied during the experimental investigation in section 3. **(b)** Dashboard dimensions. **(c)** PIV regions of interest (ROI). **(d)** Schematic depiction of pressure tap positions along windshield centerline. For interpretation of the references to color, the reader is referred to the web version of this manuscript. All dimensions are given in mm.

maximum pulse energy of 300 mJ at 532 nm, whose light beam was directed to the test section and conditioned into a light-sheet of approximately 1 mm–2 mm thickness using a light guiding arm (cf. Fig. 2). Di-Ethyl-Hexyl-Sebacic-Acid-Ester (DEHS) was used to seed the flow. The illuminated area was divided into three fields of view (FOV) with dimensions $598 \times 440\,\mathrm{mm}^2$, $280 \times 205\,\mathrm{mm}^2$ and $98 \times 78\,\mathrm{mm}^2$, representing the jet area and the interior of the primary duct, respectively. FOV 1 and 2 were captured using two LaVision Imager CX1-12 cameras featuring an $11.2 \times 8.2\,\mathrm{mm}^2$ sensor and Nikon Nikkor objectives of focal lengths $f_1 = 35\,\mathrm{mm}$ and $f_2 = 60\,\mathrm{mm}$, respectively. For FOV 3 an Imager SX-6 camera employing a $12.5 \times 9.9\,\mathrm{mm}^2$ sensor and equipped with a Zeiss Milvus objective with focal length $f_3 = 135\,\mathrm{mm}$ was used. Masking was applied to all FOVs as part of the PIV pre-processing, resulting in the three regions of interest (ROI) depicted in Fig. 3c.

Region 1 was intended primarily to identify a qualitative map, which constitutes an overview of the different jet states depending on the two main parameters β and L_s. With the state map given, individual parameter configurations were selected for a more thorough quantitative near-field analysis of the jet and the flow within the primary duct. Multi-pass cross-correlation was performed with an initial pass of $96 \times 96\,\mathrm{px}$ followed by two passes with a final interrogation window size of $32 \times 32\,\mathrm{px}$ for ROI 2 and 3 and $48 \times 48\,\mathrm{px}$ for ROI 1. A total of

3000 particle image pairs were recorded in double-frame mode for ROIs 2 and 3 in steady-state operating points and 4500 to capture a sufficient amount of switching-events for statistical analysis of bistable jet-switching.

For the state map generation, the jet behavior was qualitatively assessed in real-time via the particle seeding distribution. A minimum of 100 image pairs was then acquired for each parameter configuration for further confirmation. The dashboard position L_s was varied in 2 mm increments from 0 mm to the maximum distance of 100 mm at fixed β. In each new point, air supply was activated only after the parameters had been set to ensure unbiased formation of the jet state. A waiting time of 60 s was chosen as a sufficient time interval required for the final state to be established. After the maximum L_s value was reached, the process was repeated after incrementing the rotating disk angle by 2° using the cobot and returning the dashboard to its starting position. As described earlier, the corresponding values for β can be derived from the disk angle.

For all measurements, the repetition rate was set to 15 Hz. Synchronization between the laser and imaging systems was achieved using a LaVision programmable timing unit model X and DaVis software version 10.2. The displacement of the dashboard dummy was carried out by integrating the LaVision micro stage controller into the project interface within DaVis.

The final correlation window sizes were chosen based on the convergence of velocity and turbulent kinetic energy line profiles at various positions of the jet and within the duct (see supp. Fig. 5). Visual inspection of the particle images confirmed a displacement of roughly a quarter of the window size between frames as recommended in [55]. Similar analyses have been performed to assess the effects of denoising and filtering as part of the vector postprocessing step. Vectors with correlation values < 0.2 have been deleted and subsequently replaced by interpolation. A flowchart depicting the complete pre- and postprocessing routine is given in supp. Fig. 4.

Uncertainties of the mean velocity components were obtained in DaVis using the built-in correlation-statistics-based propagation framework [56–58]. In ROI 2, uncertainties were estimated to range from $< 0.001\,\mathrm{m\,s^{-1}}$ to $0.025\,\mathrm{m\,s^{-1}}$ and $0.032\,\mathrm{m\,s^{-1}}$, for $\langle u \rangle$ and $\langle v \rangle$, respectively, while the RMS value of the velocity magnitude was on the order of $1.57\,\mathrm{m\,s^{-1}}$. The highest values occurred in the developing shear layers just above the duct outlet, where sharp gradients are present. For ROI 3, maximum uncertainty values amount to $0.03\,\mathrm{m\,s^{-1}}$ for $\langle u \rangle$ and $0.04\,\mathrm{m\,s^{-1}}$ for $\langle v \rangle$ around the separating shear layer close to the duct inlet. Here, $\langle \cdot \rangle$ denotes temporally averaged values. Statistical convergence of the mean velocity components with increasing number of PIV snapshots was verified and is shown in supp. Fig. 6.

DEHS droplets were generated using a TSI portable test aerosol generator, model 3037, whereby the supply was split between the primary and secondary sides and controlled through manually adjusted valves. According to the manufacturer datasheet [59], the produced tracer particle mode diameters correspond to $d_{\mathrm{tr}} = 0.15$–$0.3\,\mu\mathrm{m}$. With the pixel scale for ROI 2 given as $s_{\mathrm{px}} = 68.6\,\mu\mathrm{m\,px^{-1}}$, the spatial resolution is approximated here as the final correlation window size $\Delta_{\mathrm{IW}} \approx 32 s_{\mathrm{px}} = 2.19\,\mathrm{mm}$. Together with the nominal jet velocity for $\beta = 45°$ (cf. Table 2), $U_{\mathrm{j}} = 4.2\,\mathrm{m\,s^{-1}}$, a characteristic flow timescale at the approximated resolution can be estimated as

$$\tau_f \propto \frac{\Delta_{\mathrm{IW}}}{U_{\mathrm{j}}} \approx 5.2 \times 10^{-4}\,\mathrm{s}.$$

Assuming Stokes drag for spherical particles, the Stokes number [60] with particle response time τ_p then becomes

$$\mathrm{Stk} = \frac{\tau_{\mathrm{tr}}}{\tau_f} = \frac{\rho_{\mathrm{tr}} d_{\mathrm{tr}}^2 U_j}{18 \mu_{\mathrm{air}} \Delta_{\mathrm{IW}}} \approx 1.2 \times 10^{-4} \text{ to } 4.8 \times 10^{-4} \ll 1,$$

indicating adequate tracer fidelity of the DEHS droplets for the given range of d_{tr}. Here, $\rho_{\mathrm{tr}} = 912\,\mathrm{kg\,m^{-3}}$ for DEHS [61] and $\mu_{\mathrm{air}} = 1.8 \times 10^{-5}\,\mathrm{Pa\,s}$ at 22 °C is assumed. A complete overview of imaging and acquisition parameters is provided in Table 3.

The light guiding arm was connected to an Isel linear traverse controlled via DaVis to enable spanwise displacement of the laser sheet for assessment of the two-dimensionality of the flow field inside both inflow sections, the primary duct and in the jet region. More information on the inflow measurements is provided in supp. Sec. 2 of the supplementary material. Furthermore, results of the two-dimensionality assessment of the primary duct flow and the jet can be found in supp. Sec. 3. Photographs of the defrost test rig including the Isel traverse are available in supp. Sec. 4.

Mass flow rates were measured upstream of both plena using thermal mass flowmeters Sensyflow P from ABB with an accuracy of $< \pm 1\%$ of reading. This data was collected at a sampling rate of 20 Hz during all PIV investigations through an ETAS electronic control unit (model ES892.1), monitored and stored using ETAS INCA version 7.4 software.

Subsequent to the PIV investigations, pressure measuring points in the form of 71 tubes, each with a diameter of 1.9 mm and spaced 4 mm apart, were installed over a distance of 280 mm along the windshield center line, see Fig. 3d. Individual measuring points were connected to a Scanivalve pressure scanner (type Digital Sensor Array 3217/16Px) using Vinnylan tubing. Each of the six arrays, also referred to as modules, consists

of 16 differential pressure transducers with a full-scale range of ±10 inH_2O (≈ ±2490 Pa) and a specified static accuracy of ±0.20% of full scale (±5 Pa). Measurements were acquired in gauge mode (i.e. referenced to ambient atmospheric pressure) with the common reference routed to a quiescent corner of the laboratory, sufficiently removed from the defrost jet to avoid flow-induced disturbances. The modules are connected to the computer via an Ethernet switch, with the data acquisition performed using an in-house National Instruments LabVIEW program. To reduce zero-offset bias, a rapid in situ zero calibration was performed prior to each measurement by pneumatically shorting the sensor ports. Pressures were then recorded at 50 Hz for 300 s (15 000 samples) in steady-state flow and averaged over the full record. The standard error of the mean (SEM) was estimated via block averaging with a block-size of 10 s to account for temporal correlation of the samples. Across all channels and measurement cases, SEM values ranged from 0.0013 Pa to 0.095 Pa, with a 95^{th}-percentile SEM of 0.021 Pa.

Table 3: Overview of PIV imaging and acquisition setup.

	Model | Value		
Instrument | Parameter	**ROI 1**	**ROI 2**	**ROI 3**
Camera	LaVision Imager CX1-12	LaVision Imager CX1-12	LaVision Imager SX-6M
Lens (mount)	Nikon AF-S 28-70 mm 2.8 D IF ED	Nikon AF 60 mm 2.8 D Micro	Zeiss Milvus 2/135
Aperture f/#	f/4	f/4	f/4
Object distance	1370 mm	1400 mm	970 mm
Calibration/scaling method	2D calibration plate	2D calibration plate	Ruler-based scaling
Calibration target	134-12 SSSP	80-8 SSSP	-
Scale factor	8.48 px mm^{-1}	14.58 px mm^{-1}	28.02 px mm^{-1}
Pixel size in object space	117.9 μm px^{-1}	68.6 μm px^{-1}	35.7 μm px^{-1}
Correlation window (final pass)	48 × 48 px	32 × 32 px	32 × 32 px
Window overlap (final pass)	75%	75%	75%
Vector spacing	1.42 mm	0.549 mm	0.286 mm
Correlation window width	5.66 mm	2.19 mm	1.14 mm
Particle image density	0.025–0.068 ppp	0.025–0.04 ppp	0.033–0.066 ppp
Number of image pairs	100	3000, 4500	3000
Pulse separation dt	100 μs	100 μs	30 μs

2.3 Jet-Flow Terminology and Definitions

For the sake of clarity, we would like to introduce some terminology that is frequently encountered in the context of wall-attaching/plate-impinging jet flows, with reference to Fig. 4. According to Hoch and Jiji [63], the primary jet exiting the defrost duct is subdivided into three regions. In the pre-attachment region (cf. Fig. 4a), the airstream resembles a free jet including a potential core within which the centerline velocity is equal to the mean velocity at the duct exit. Here and in the following, the jet centerline is defined as the locus of maximum velocity. On both sides of the centerline, two shear layers steadily growing in- and outwards along the streamwise direction. The potential core extends up to the point of shear layer merging that marks the onset of centerline velocity decay. Due to the continuous entrainment of ambient air into the jet, air from further outside is drawn in, creating a backflow to compensate for the associated pressure reduction. Proximity to nearby surfaces causes acceleration of the entrained air, thereby giving rise to a pressure gradient oriented transversely to the jet axis and resulting in deflection of the jet towards the surface [64]. This phenomenon is commonly known as the Coandă effect. Between the jet and the respective surface, a recirculation zone develops.

From the stagnation point onwards (cf. Fig. 4c), a realignment of the jet along the wall-parallel direction takes place within the impingement region, whereby the oblique attachment causes a bifurcation into oppositely oriented branches of different momenta. The main part of the jet evolves into a plane wall jet (WJ, cf. Fig. 4b), which is traditionally described by a two-layer structure [62]. The inner layer (IL) ranges from the wall to the location of the velocity maximum. Although often regarded as boundary-layer-like, the IL appears to be more complex than a conventional turbulent boundary layer because it remains influenced by outer jet dynamics [65]. Due to residual near-wall laser reflections during the PIV measurements, the IL is not considered in the present study. Above the velocity maximum, the jet-dominated outer layer (OL) extends away from the wall. Following Pelfrey and Liburdy [66], a local positive η-ξ coordinate-system aligned with the jet centerline is defined, whereby η measures the distance from the primary duct exit along the centerline and ξ is orthogonal to it. The outward normal distance from the centerline to the position where the velocity is equal to one-half of the local maximum velocity is termed the outer half-width $\delta^{\text{o}}_{1/2}$ of the jet. In addition, in the free-jet region, the inner half-width $\delta^{\text{i}}_{1/2}$ characterizes the shear layer on the side of the surface the jet is attached to.

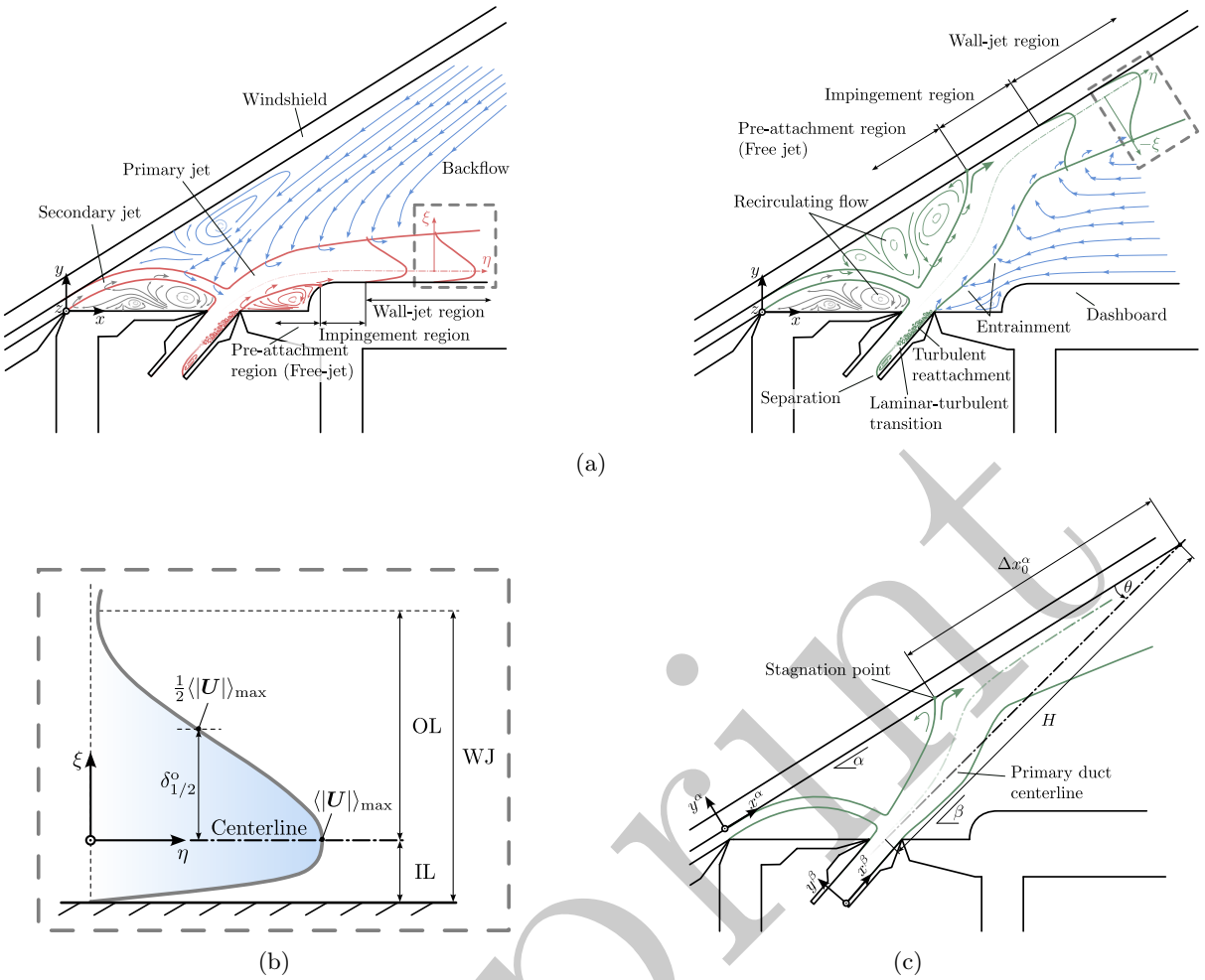

Fig. 4: **(a)** Schematic representation of the fundamental flow topology and phenomena. **(b)** Traditional two-layer structure of the turbulent plane wall-jet (WJ) [62] with definition of the local jet centerline (η-ξ) coordinate system. IL: Inner layer. OL: Outer layer. **(c)** Definition of the stagnation point eccentricity Δx_0^α.

Auxiliary coordinate systems x^α-y^α and x^β-y^β are introduced to describe the flow on the surface of the windshield and within the primary duct, respectively (cf. Fig. 4c). The virtual extension of the duct axis intersects the windshield at a distance H and at an angle $\theta = \beta - \alpha$. The difference between this intersection point and the position of the stagnation point defines the stagnation point eccentricity Δx_0^α.

3 Results and Discussion

3.1 State Map and Jet Hysteresis

Figure 5a summarizes the results of the qualitative flow state identification as a function of the primary duct angle β and dashboard distance L_s. In total, seven states are distinguished, whereby the classification is purely qualitative due to gradual transitions between neighboring configurations. A PIV snapshot of the instantaneous velocity magnitude in each state is depicted in Fig. 5b and described hereafter.

Windshield-deflected (ws-def) is characterized by statistically steady-state windshield-attached flow that also exhibits partial attachment along the front of the dashboard. In windshield (ws) states, the jet is fully attached to the windshield, that is without any contact to the dashboard. Contrarily, states dashboard-A (db-A) and dashboard-B (db-B) are defined by complete attachment to the dashboard (i.e. over its entire upper surface). In operating points designated as dashboard-separating (db-sep), weak attachment to the upper dashboard surface is noticed with the possibility of occasional separation. However, no deflection towards the windshield occurs. Parameter configurations marked as state-switching (ssw), show aperiodic alternating behavior of the jet between dashboard-attached flow (db-A or db-sep) and windshield attachment (ws or ws-def). Likewise, random fluctuations between ws-def and ws are observed in the windshield-fluctuating state (ws-fluct) (see Fig. 5e for a detailed view).

Several characteristic regions can be discerned from the map. For steep duct angles, predominantly windshield-attached states are encountered, whereby a transitional stripe consisting of ssw and ws-fluct configurations separates ws-def from ws. At the steepest β values, sporadic dashboard attachment in the form of ssw is not detected. As the angle decreases, the influence of the dashboard steadily increases, causing the jet to be deflected by its presence at progressively larger values of L_s. Eventually, a region of dashboard-attached flow emerges and expands over moderate dashboard distances. This region is bounded by db-sep and ssw configurations and contains the two variants of dashboard attachment, db-A and db-B. For β and L_s within this monostable region, the jet invariably attaches to the dashboard. Transitions between db-A and db-B can occur spontaneously and both can remain stable for significant periods of time within the monostable range. State db-A is characterized by saturation with tracer particles trapped within the ROI, caused by a large-scale recirculation downstream of the dashboard. This recirculation presumably originates from partial detachment of the jet from the dashboard at lateral positions offset from mid-span, leading to nearby dashboard-attached prtions of the jet to be deflected back into the ROI (cf. Fig. A1a). For state db-B, the background particle density is noticeably reduced, indicating dashboard-attachment across the entire span with backflow consisting of tracer-poor ambient air from outside the windshield. Within the scope of a 2D2C PIV measurement campaign it is, however, not possible to conduct an in-depth analysis into the three-dimensional structure of the flow, meaning that the root cause of the two states could not be conclusively clarified. A more thorough discussion regarding their characteristics is given in Appendix A.

State db-B persists for parameter values beyond the monostable range, where spontaneous dashboard attachment does not occur. On the contrary, in these points db-A gradually transitions towards the windshield within 10–40 s. The hysteresis associated with db-B therefore reveals bistable configurations capable of sustaining both dashboard- and windshield-attached flow. Sample checks showed that dashboard attachment can persist for as long as 10 min in bistable points (longer tests have not been conducted). Figures 5c and 5d summarize the extent of this hysteresis. The maximum duct angle $\beta_{\mathrm{max,db}}$ and the dashboard position interval $\Delta L_{s,\mathrm{db}} = L_{s,\mathrm{max,db}} - L_{s,\mathrm{min,db}}$ at which dashboard-attached flow was observed increase significantly beyond the monostable range. With increasing β or L_s, however, the values for $L_{s,\mathrm{max,db}}$ and $\beta_{\mathrm{max,db}}$ due to hysteresis decrease accordingly, as configurations above these values became unstable and transitioned to windshield attachment after a short period of time during the experiments. This does not imply that dashboard attachment beyond these limits is impossible, but rather that even with a nominally two-dimensional setup the probability for detachment at some location along the span increases with β and L_s, triggering total detachment from the dashboard outside of the monostable range.

Figure 6 illustrates the contrast between the spontaneous and hysteretic behavior of the jet along the $\beta = 45°$ row of the state map. The top row shows states that the jet attains spontaneously, that is without prior conditioning. The arrows indicate that these states arise either when the air supply is initiated with the corresponding parameters preset, or when the parameters are varied from any other state except db-B while the blowers remain active. The bottom row represents the hysteretic response: once the jet reaches state db-B within the monostable regime and the dashboard is subsequently traversed, the ability of the flow to remain attached to the dashboard even outside the monostable range significantly increases, indicating bistability. Alternatively, the duct angle β can be varied to achieve the same effect and provoke the Coandă effect at steeper angles for constant L_s (not shown).

3.2 Characteristics of the Mean Flow

3.2.1 Windshield Surface Pressure Distribution

The wall static pressure distribution along the windshield centerline was measured for various dashboard positions and three primary duct angles of $\beta = 45.0°$, 61.9° and 80.6°. Figure 7 shows the pressure coefficient defined as

$$c_p = \frac{p_\mathrm{w} - p_\infty}{\frac{1}{2}\rho_\mathrm{air} U_\mathrm{j}^2} \tag{1}$$

plotted against the normalized wall-parallel coordinate $x^\alpha / L_{d,\mathrm{eff}}$ for windshield-attached flow. Here, $p_\mathrm{w} - p_\infty$ denotes the measured relative surface pressure, where p_∞ is the ambient reference pressure. The air density is taken as $\rho_\mathrm{air} = 1.2\,\mathrm{kg\,m^{-3}}$, corresponding to sea-level conditions at 20 °C, and U_j denotes the nominal jet exit velocity listed in Table 2. The pressure coefficient distribution for $\beta = 45.0°$ is consistent with the patterns reported in the literature for oblique wall-attaching offset jets (OWAOJ) and oblique-plate impinging jets (OPIJ) with shallow impingement angles. A region of sub-atmospheric static pressure is followed by a minimum, a sharp increase to the peak value, and a subsequent pressure recovery farther downstream. The sub-atmospheric plateau and pressure minimum within the cavity bounded by the jet, windshield and cover plate indicate a recirculation zone upstream of the stagnation point. As noted by Beltaos [69], at shallow impingement angles, part of the minor branch of the bifurcating jet is entrained into the inner shear layer of

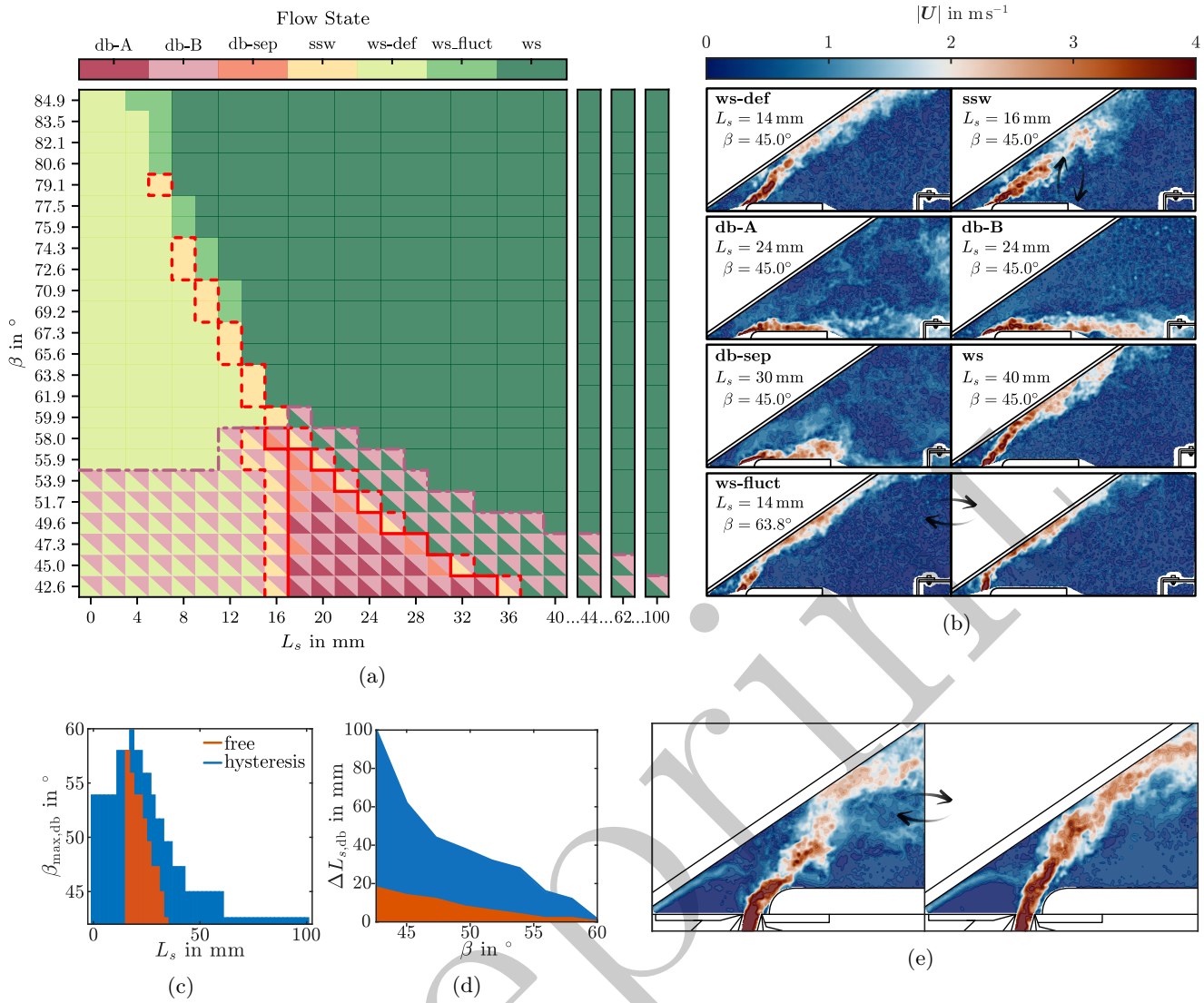

Fig. 5: **(a)** Primary jet state map as a function of primary duct angle β and the distance between duct exit and dashboard L_s (cf. figure 3). **ws-def**: Windshield attached state deflected by dashboard. **ssw**: State-switching. **db-A**/**B**: Full dashboard attached states. **db-sep**: Dashboard attached state close to separation. **ws**: Windshield attached state without contact to dashboard. **ws-fluct**: Fluctuating between ws-def and ws. — Region within which only dashboard attachment has been observed. -- Region within which spontaneous reattachment to the dashboard has been observed. -·- Maximum region within which dashboard attachment has been observed due to hysteresis. **(b)** Exemplary instantaneous PIV snapshots of individual states. **(c)** Maximum primary duct angle for which dashboard-attached flow has been observed. **(d)** Maximum interval of dashboard distances for which dashboard-attached flow has been observed. **(e)** Close-up view of state **ws-fluct** (bottom row in subfigure b).

the free-jet, thereby creating a vortical flow that imposes low surface pressure. Thereafter, deceleration and redirection of the jet during impingement cause a rapid pressure rise. As the flow gradually develops into a wall jet, the pressure relaxes toward ambient levels. With the dashboard distance increasing from $L_s = 8$ mm to $L_s = 14$ mm, the jet remains attached to the front part of the dashboard (state ws-def, cf. 5a). Consequently, the extrema shift downstream, with the minimum value remaining nearly unchanged while the peak value decreases significantly. In addition, the distribution broadens with more gradual pressure rise and recovery on either side of the maximum. This indicates stronger deflection of the jet from the windshield including an extended recirculation zone and correspondingly weaker impingement on the windshield. Beyond the monostable range ($L_s = 40$ mm and $L_s = 100$ mm), the influence of the dashboard continuously diminishes and the pressure distribution resembles the pattern seen for $L_s = 8$ mm. This similarity suggests a marginal effect of the dashboard for the specific position in the latter case.

Experimental data from a study conducted by Song et al. [67] on an OWAOJ with an offset-to-nozzle-width ratio of $L_b/L_{d,\mathrm{eff}} = 5$ (denoted as H/D in the reference) are included for comparison. To facilitate the comparison, the impingement angle θ is used alongside the duct angle. According to the remarks in Sec. 1,

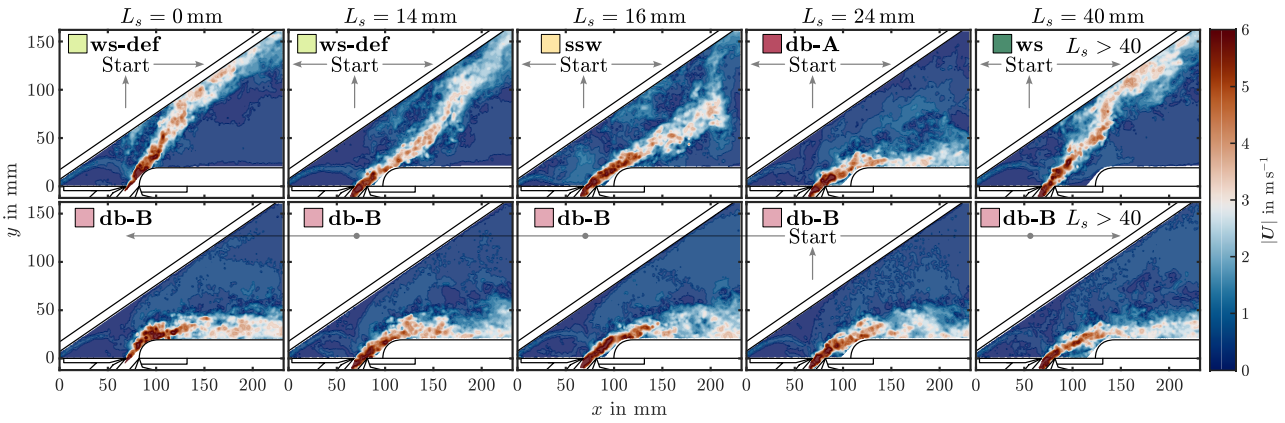

Fig. 6: Instantaneous velocity magnitude displaying hysteresis in the primary jet behavior due to the Coandă effect (duct angle fixed at $\beta = 45.0°$ and varying L_s). Top: Spontaneously emerging primary jet state for each value of the dashboard distance L_s, appearing when the air supply is enabled at fixed parameters or when approached from any other state corresponding to those of the top row through a variation of β or L_s with uninterrupted air supply. Bottom: Hysteretic dashboard attachment, when each point is approached from state db-B. An explanation of the jet state abbreviations can be found in the caption of Fig. 5.

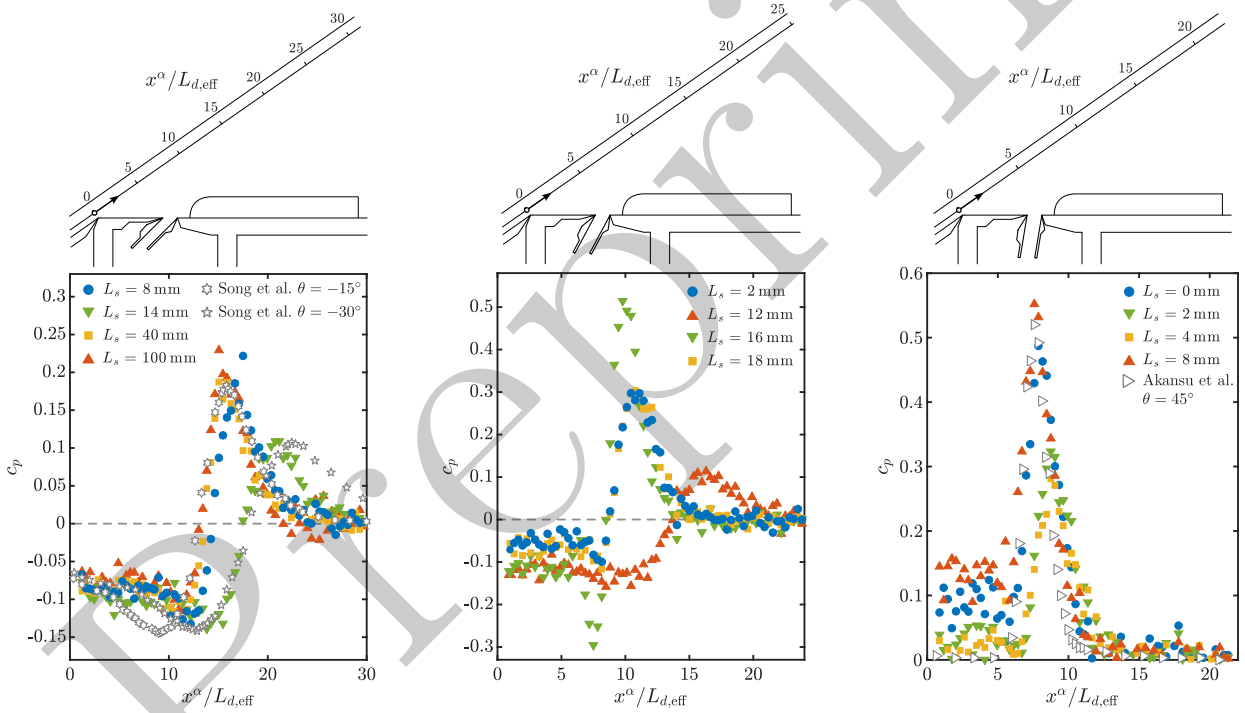

(a) $\beta = 45.0°$ ($\theta = 10.0°$) (b) $\beta = 61.9°$ ($\theta = 26.9°$) (c) $\beta = 80.6°$ ($\theta = 45.6°$)

Fig. 7: Pressure coefficient distribution on windshield surface for windshield-attached states. Reference values correspond to studies of an oblique wall-attaching offset jet, Song et al. [67] (offset-to-duct-width ratio $L_b/L_d = 5$) and an oblique-plate impinging slot jet, Akansu et al. [68] (plate-spacing-to-duct-width ratio $H/D_\mathrm{h} = 6$). D_h corresponds to the hydraulic diameter of the slot used in the latter reference.

the windshield-attached flow here technically classifies as an OPIJ with a very shallow impingement angle of $\theta = 10.0°$. Note that the angles from the OWAOJ reference become negative under the definition for θ given in Fig. 4c. The agreement with the reference data confirms that for windshield attachment at low duct angles the flow corresponds to a Coandă-dominated wall-attaching jet. Furthermore, proximity to the dashboard can affect the pressure distribution in a similar way to a reduction in the plate inclination angle in the reference case, which translates to a reduction of the duct angle β in the present study. This has direct implications for the heat-transfer characteristics of the defrost jet, since the reported effects on the surface pressure are reflected in the local Nusselt number distribution. A broadening, downstream shift and reduction of the pressure peak indicate a downstream-shifted and weaker maximum in the Nusselt number, spread across a wider area (cf. Figs. 2 and 9 in [67]).

Similar behavior is observed for a primary duct angle of $\beta = 61.9°$, although overall the pressure coefficient peak values increase due to a larger wall-normal momentum component compared to the lower angle. Despite being located in the ws region of the state map, the pressure distribution for case $L_s = 16\,\text{mm}$ exhibits a noticeable influence of the dashboard as a result of close proximity. The profile suggests stronger impingement and a more pronounced vortex formation, the origin of which is further examined using the velocity field analysis in Sec. 3.2.2. On the contrary, the maximum reduces by approximately 78% for $L_s = 12\,\text{mm}$, again indicating downstream deflection caused by the partial attachment to the dashboard.

At a duct angle of $\beta = 80.6°$, the transition from a Coandă-dominated to an impingement-dominated regime is completed. Data from a study by Akansu et al. [68] of an oblique-plate impinging slot-jet is included for reference. The effect of entrainment in the pre-attachment region is now outweight by deceleration of the impinging jet, leading to a build-up of positive static pressure compared to the cases with shallower duct angle. Note that the reference pressure coefficient remains at the ambient level upstream of the maximum because the reference experiment employs an open setup, in which the jet does not form a cavity with the plate as in the present configuration. Again, a significant influence of the dashboard position is noticed, leading to a narrower pressure profile and a reduction of the peak value by 49% between $L_s = 8\,\text{mm}$ and $L_s = 4\,\text{mm}$.

Pressure coefficient peak values below unity indicate transitional impingement for all investigated configurations, although the existence of a distinct potential core is examined in the subsequent section using PIV data.

3.2.2 Mean Velocity and Turbulent Kinetic Energy Fields

Table 4: Stagnation point location x_0^α and eccentricity Δx_0^α for windshield-attached states.

Present study	L_s **in mm**	x_0^α/L_w **in %**	$\Delta x_0^\alpha/H$	**Reported values**	$\Delta x_0^\alpha/H$
$\beta = 80.6°$ $(\theta = 45.6°)$	0	11.7	-0.09		-0.19 Eq. (3)
	2	12.6	0.02	$\theta = 45.0°$	-0.25 [70]
	4	13.6	0.14		-0.19 [71]
	8	11.5	-0.12		
$\beta = 61.9°$ $(\theta = 26.9°)$	2	13.9	-0.33		-0.42 Eq. (3)
	12	20.7	0.22	$\theta = 30.0°$	-0.53 [70]
	16	13.3	-0.38		-0.34 [71]
	18	14.0	-0.33		
$\beta = 45.0°$ $(\theta = 10.0°)$	0	14.8	-0.74		
	8	18.4	-0.63		
	14	22.5	-0.50		
	34	16.2	-0.70		
	40	17.5	-0.66		
	100	17.2	-0.67		

Table 5: Exponents of the power-law regression to the centerline velocity decay ζ for windshield-attached states. Data from [70] of an oblique-plate impinging slot jet with a nozzle-to-plate spacing ratio $H/B = 4$ is included for reference (B is the slot width within the reference).

Present study	L_s **in mm**	ζ	**Zhang et al. [70]**	**Re**	ζ
$\beta = 80.6°$ $(\theta = 45.6°)$	0	-0.36	$\theta = 45.0°$	3000	-0.39
	2	-0.25		6000	-0.34
	4	-0.19			
	8	-0.37			
$\beta = 61.9°$ $(\theta = 26.9°)$	2	-0.26	$\theta = 30.0°$	3000	-0.34
	16	-0.40		6000	-0.28
	18	-0.23			
$\beta = 45.0°$ $(\theta = 10.0°)$	0	-0.38			
	8	-0.21			
	34	-0.32			
	40	-0.24			
	100	-0.26			

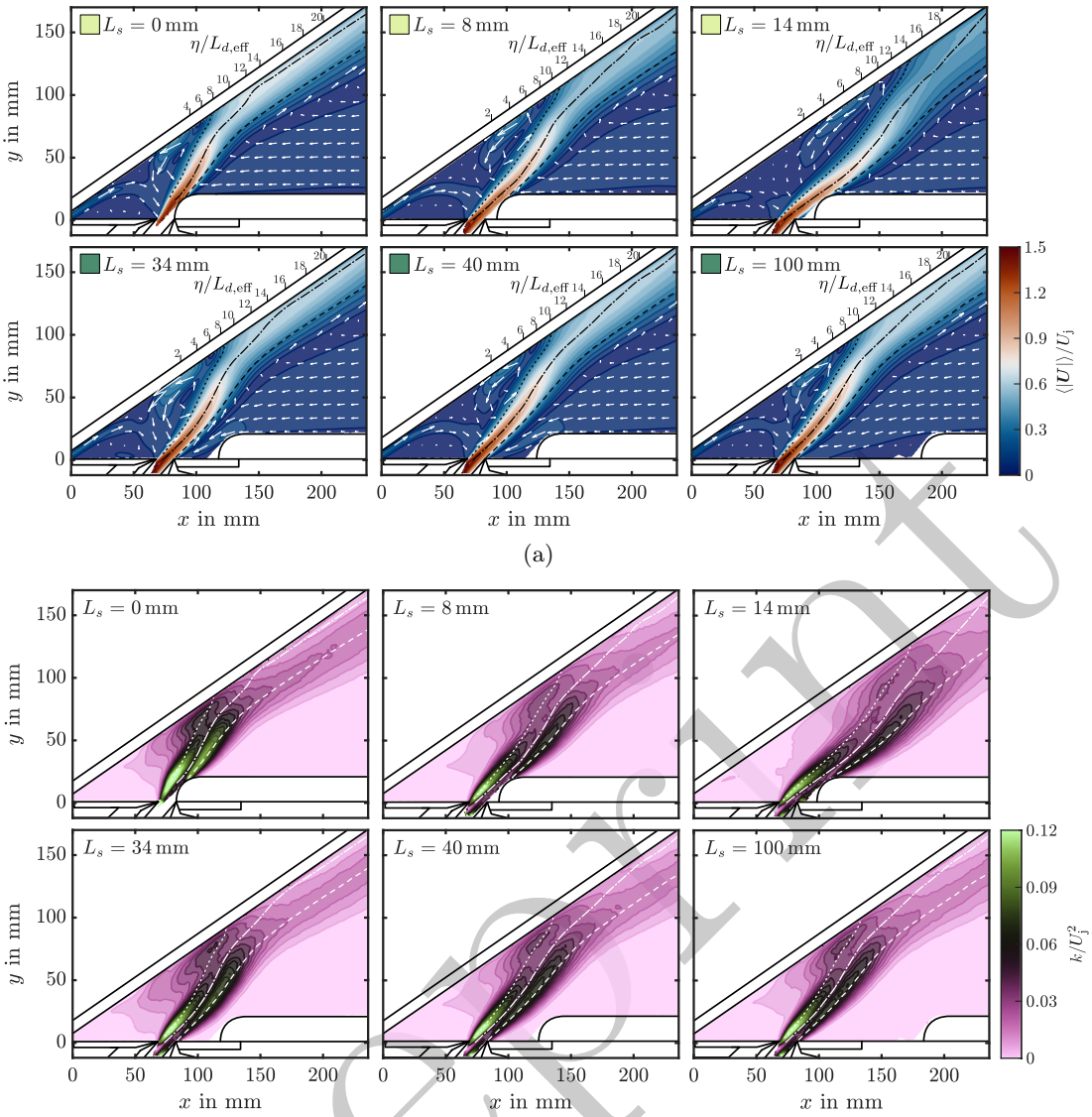

Fig. 8: Normalized time-averaged velocity magnitude **(a)** and turbulent kinetic energy **(b)** contours for windshield-attached states. ▪▪▪ Inner half-width. ▬▬ Outer half-width. ▪▪▪ Primary jet centerline.

Contours of the time-averaged velocity magnitude normalized by the nominal jet exit velocity are shown in Fig. 8a for windshield-attached flow with a primary duct angle of $\beta = 45.0°$ and various dashboard positions. The dash-dotted centerlines are obtained by fitting piecewise cubic Hermite interpolating polynomials through the loci of maximum velocity using MATLAB's built-in PCHIP function. Line markers on the windshield indicate the distance from the duct exit along the centerline. The given values correspond to the intersection points between the vertically extended markers and the centerline. The half-width locations are determined by outward normal projection to the points where the velocity equals half the local maximum and are likewise approximated using PCHIP (dotted and dashed lines denote the half-widths of the inner and outer shear layer, respectively).

The PIV results support the interpretation of the pressure profiles given in the previous section. As the jet partially attaches to the front part of the dashboard, its trajectory is substantially altered. At the stagnation point, the jet bifurcates into a major and minor branch, the latter of which merges with the secondary jet before being entrained into the free jet, forming the vortex structure that was previously associated with the pressure minima in Fig. 7. For a dashboard position of $L_s = 34$ mm, the jet is right outside of the monostable regime (cf. 5a). However, the close proximity leads to accelerated backflow between the jet and the front part of the dashboard, as is indicated by the vector lengths. The accompanied pressure reduction within this gap causes the free jet to bend outwards, which in turn affects the impingement angle. Consistent with the steeper jet inclination and increased entrainment demand immediately above the duct exit as a consequence of the accelerated backflow, a more energetic minor branch is created that is entrained again into the approaching jet, forming a stronger low-pressure vortex. This effect is also observed for increased duct angles (cf. Fig. B1a)

and explains the more pronounced pressure extrema encountered in the case with $L_s = 16\,\mathrm{mm}$ and $\beta = 61.9°$ discussed in Sec. 3.2.1. The previously described changes in the extent of the pressure variations correlate with the length of the impingement zone, which is here loosely defined as the region between the first right-hand bend of the centerline to its full wall-parallel reorientation. Between the minimum and maximum dashboard positions, the impingement zone grows roughly from 8–12 $\eta/L_{d,\mathrm{eff}}$ to 10–20 $\eta/L_{d,\mathrm{eff}}$.

Figure 8b shows the corresponding contours of normalized turbulent kinetic energy (TKE). With the spanwise velocity fluctuations w' not available in 2D2C PIV, TKE is estimated using a pseudo-isotropic assumption [72]:

$$k = \frac{3}{4}\left(\langle u'u'\rangle + \langle v'v'\rangle\right), \tag{2}$$

where u' and v' denote the fluctuating velocities along the global x and y coordinates, respectively. The highest TKE levels are present in the shear layers within the free-jet region. As the jet issues from the primary duct, the inflectional velocity profile across the shear layers makes the flow susceptible to Kelvin–Helmholtz instability, leading to growth of shear-layer disturbances and increased turbulence production. Discrepancies between the inner and outer shear layer are attributed to two factors. First, higher TKE in the inner layer (left of the centerline) right above the primary duct exit is the result of differences in the upstream boundary layer development, cf. supp. Fig. 5b in the supplementary material. The internal flow field is governed by the presence of a separation bubble on the right duct wall. TKE increases abruptly within the separated shear layer and remains elevated after subsequent reattachment. Such a pattern is a strong indication of transition to turbulence or at least substantial transitional breakdown and results in a bulkier velocity profile close to the exit, compared with the thin boundary layer on the opposite side. Consequently, the emerging jet forms a sharper left shear layer that is more susceptible to instability growth. Additionally, the highly unsteady merging of the secondary and primary jet in this region contributes to the TKE. Further downstream the situation reverses, as higher TKE is found in the outer shear layer due to asymmetric distribution of turbulent shear stress between both sides. This finding aligns with PIV measurements of an inclined plane jet reported by Ruiz et al. [73] and is amplified here by proximity of the inner shear layer to the windshield. Rapid deceleration and turning of the flow in the stagnation zone are associated with an increase in normal strain and stresses, which intensify turbulence [74]. As a result, a local TKE maximum develops that shifts toward either the minor or major branch as a function of duct angle and dashboard position. Elevated turbulence intensity in the stagnation zone and its displacement with the impingement angle were previously reported by Yoon et al. [75] for an OPIJ. As the flow evolves into a wall jet, the highest TKE levels occur in the vicinity of the outer-layer half-width and quickly decay towards the centerline and near-wall region, where vortical structures are damped by the presence of the windshield.

Taking into account the deflection of the jet towards the windshield, stagnation point eccentricity for transitional impingement of oblique jets can be approximated by [69]:

$$\Delta x_0^\alpha = \frac{-2.15\,(1 - \theta/90°)}{8\sin\theta} \tag{3}$$

A summary of the stagnation point eccentricity for the three duct angles discussed above is given in Table 4. Satisfactory agreement is found with Eq. 3 and literature values outside the sphere of influence of the dashboard. Since Eq. 3 is limited to $30° \leq \theta \leq 90°$ and a literature search by the authors yielded no results for $\theta = 10.0°$ ($\beta = 45.0°$), no comparison is possible for that case. Due to the partial attachment to the dashboard, the eccentricity shifts significantly depending on the exact position of the dashboard and even changes sign. Moreover, the wide spread in eccentricity with impingement angle, compared to the narrow range of values of the relative stagnation point location x_0^α/L_w, again emphasizes the dominant role of the Coandă-induced flow attachment on the windshield side for shallow angles.

Figure 9 shows selected contours of time-averaged velocity magnitude and TKE for dashboard-attached flow. Considering the settlement and acquisition time together, the jet remained in state db-B for 5 min total, which highlights the potential for stable dashboard attachment outside the monostable regime. A cavity is formed between the jet, upper plate and dashboard that is only partially illuminated due to the oblique incidence angle of the laser light. Nevertheless, a region of recirculating flow becomes recognizable with increasing dashboard position, in which the minor jet branch diverts from the stagnation point and is then entrained at the duct exit. The sub-ambient pressure associated with this recirculation zone, together with the near-ambient pressure in the backflow-dominated region resulting from the open setup, establishes a pressure gradient that promotes dashboard attachment. On the upper part of the dashboard front, an acceleration region is present that becomes weaker with increasing dashboard distance, suggesting a downstream drifting of the stagnation point along the curved surface.

Turning to the TKE contours, noticeably higher turbulence levels are observed for the configuration with zero dashboard distance. The strong streamline curvature over the front part in this case, with a distinct

outer-layer TKE peak is consistent with reported behavior for turbulent wall jets over convex surfaces [76]. As the dashboard is shifted towards larger distances, elevated outer-layer TKE levels spread progressively in the horizontal direction. This observation is revisited below in the discussion of maximum velocity decay and half-width growth rates.

Figure 10 shows the centerline velocity, defined as

$$U_\mathrm{c} = \langle |\boldsymbol{U}| \rangle \, (\eta, \xi = 0) \,, \tag{4}$$

normalized by the maximum velocity at the duct exit $\widehat{U}_\mathrm{c} = U_\mathrm{c} \, (\eta = 0)$, as a function of the streamwise distance. For zero dashboard distance, the exit velocity is taken from the $L_s = 8\,\mathrm{mm}$ case due to the shadow caused by the oblique light incidence angle. Data from Yoon et al. [77] for a plane wall jet (PWJ) and wall-attaching offset jet (WAOJ) is included for reference. The windshield-attached flow in Figs. 10a, 10c and 10d displays the typical WAOJ decay variation with a $-1/2$ slope in the free-jet region, followed by a local minimum in the stagnation zone where the jet decelerates. Thereafter, the favorable streamwise pressure gradient (cf. Fig. 7) results in acceleration as the jet is compressed in cross-stream direction and reorients into a wall jet. Ultimately, mixing with ambient fluid and subsequent spreading cause the wall-jet centerline velocity to diminish again.

The potential core length is commonly defined as the distance from the duct exit, where the normalized centerline velocity reaches 90% [78] after a noticeable plateau. This 90% threshold is indicated in Fig. 10 by the light-red region. Compared to the reference, no plateau can be discerned in the present measurements as the centerline already decays at the duct exit (note also the difference in abscissa scaling). This is attributed to the conditioning of the jet by a contraction nozzle, yielding a nearly uniform exit velocity profile in the reference experiments in contrast to the developing, non-uniform duct exit profile observed here (cf. supp. Fig. 5b). For the specific case of zero dashboard distance, the elevated centerline velocity in the beginning results from acceleration of the flow over the quarter-cylindrical dashboard front part.

Shortly upstream the local minimum, a faster decay is noticed for the cases in Fig. 10a and 10c, compared to the cases with $\beta = 80.6°$ in Fig. 10d, for which the local minimum is approached approximately at the canonical free-jet decay rate of $-1/2$. The former configurations exhibit sub-ambient pressure and a pronounced minimum in Fig. 7. One plausible interpretation is that the associated near-wall vortex formation contributes to the centerline velocity decay by extracting momentum from the approaching jet in the pre-attachment region. This is further supported by the steepest pre-impingement decay occurring for the configurations with $L_s = 34\,\mathrm{mm}$ in Fig. 10a and $L_s = 16\,\mathrm{mm}$ in Fig. 10c in view of their previous discussion.

In the wall-jet region, decay rates ζ are indicated by the slopes of the dash-dotted lines and calculated from power-law regressions in the form of

$$\frac{U_\mathrm{c}}{\widehat{U}_\mathrm{c}} = \left(\frac{\eta}{L_{d,\mathrm{eff}}} \right)^{\zeta}, \tag{5}$$

with data included in the curve fit beginning from the onset of approximate self-similarity of the outer-scaled mean velocity profiles (cf. Appendix C). Reynolds stresses were examined as a supporting diagnostic to ensure that the selected values were not affected by strong development effects. Moreover, at finite Reynolds number, the profiles generally retain some Reynolds-number dependence, so exact collapse of all quantities is not expected over any finite downstream interval [79]. Table 5 summarizes the decay rates for the cases of windshield attachment. The calculated decay rates differ from the canonical wall-jet value of $-1/2$ predicted by dimensional analysis, indicating incomplete self-similarity [80] in the jet near-field. Beyond the range of direct contact with the dashboard, the measured decay rates are consistent with values reported in [70] for an OPIJ with $\theta \leq 45°$. Depending, on whether the dashboard deflects the jet away from or toward the windshield, a noticeably faster or slower decay is observed, respectively.

Figure 10b shows the centerline velocity decay for dashboard attached flow with a duct angle of $\beta = 45°$ and as a function of the dashboard distance. An overshoot in the centerline velocity is observed for the case with zero dashboard distance. This variant exhibits the strongest impingement and subsequent streamline curvature, since the emerging jet directly collides with the dashboard front and then makes a sharp turn onto its top side. A pronounced stagnation point in combination with the radially increasing pressure necessary to sustain the Coandă effect produce a favorable streamwise pressure gradient accelerating the jet. As was noticed from the contours of velocity magnitude and is now expressed in the decay curves, the stagnation point drifts downstream along the curved surface for increasing dashboard distance. At the same time the centerline velocity progressively decays, leading to a weaker impingement, acceleration and peak velocity.

Similar to the windshield-attached states, decay rates in the wall-jet region reveal a clear dependence on the upstream attachment process that is controlled here by the parameter L_s. For large L_s, the extent of the reattaching free-jet region together with the low-pressure pocket beneath the jet increase, so that more ambient air is entrained, which is accompanied by more significant decay and growth rates [81]. This aligns with the more energetic outer layers in the TKE contours for these cases in Fig. 9b. Enhanced turbulent mixing results

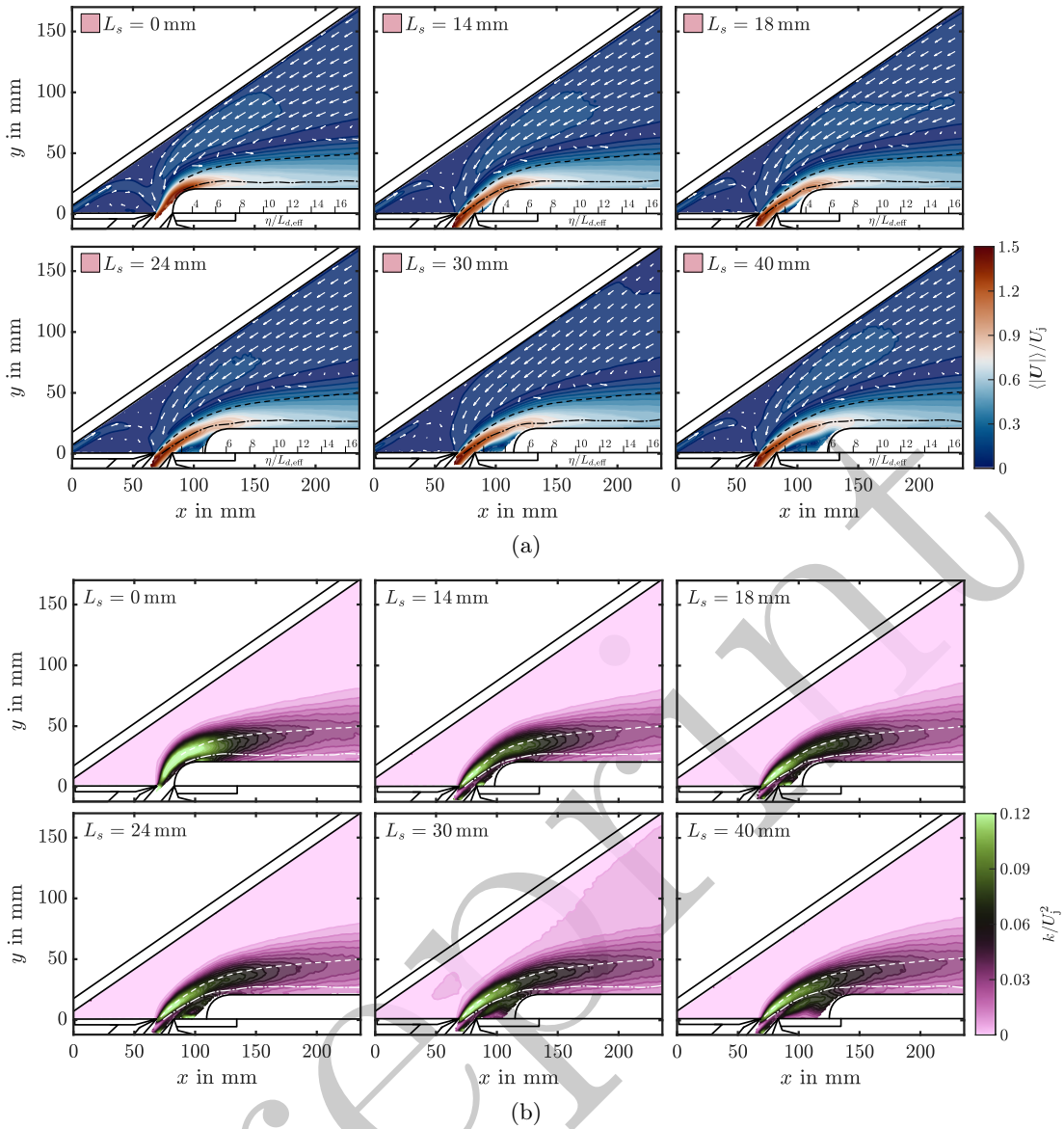

Fig. 9: Normalized time-averaged velocity magnitude **(a)** and turbulent kinetic energy **(b)** contours for dashboard-attached states in mono- and bistable configurations. **--** Outer half-width. **-·-** Primary jet centerline.

in a more rapid growth of the outer shear layer, which in turn causes a faster centerline velocity decay, as the jet momentum is redistributed over a wider cross-stream extent. To support this view, outer half-width growth rates in the wall-jet region are determined. Analogous to the decay rates, growth rates χ are expressed as exponents of power-law regressions to the wall-jet half-width variations shown in Fig. 11:

$$\frac{\delta^\mathrm{o}_{1/2}}{L_{d,\mathrm{eff}}} = \left(\frac{\eta}{L_{d,\mathrm{eff}}}\right)^{\chi}. \tag{6}$$

A reference slope corresponding to the linear growth predicted by classical asymptotic theory for plane free jets and wall jets is included. Data is included in the curve fit beginning from the onset of approximate self-similarity of the outer-scaled mean velocity profiles (cf. Appendix C) with Reynolds stresses as a complementary measure. The jet sustains approximate linear growth in the pre-attachment and impingement region up to $\eta/L_{d,\mathrm{eff}} \approx 9$ for all cases. Afterwards, sublinear outer-layer spread is seen in the wall jet. In alignment with the previous observations, growth rates in this region become progressively faster with increasing dashboard distance. An overview of the determined decay and growth rates for dashboard attachment is given in Table 6. Stronger decay and growth, together with enhanced entrainment [82], reduce jet throw, thereby weakening the Coandă effect, which is in accordance with the increased probability for early detachment with increased L_s and β mentioned in Sec. 3.1.

Half-width variations for the inner and outer shear layers of windshield-attached flow are provided in Appendix D. It is interesting to note that in the pre-attachment region (ranging from $\eta/L_{d,\mathrm{eff}} \approx 8$ for $L_s = 0\,\mathrm{mm}$

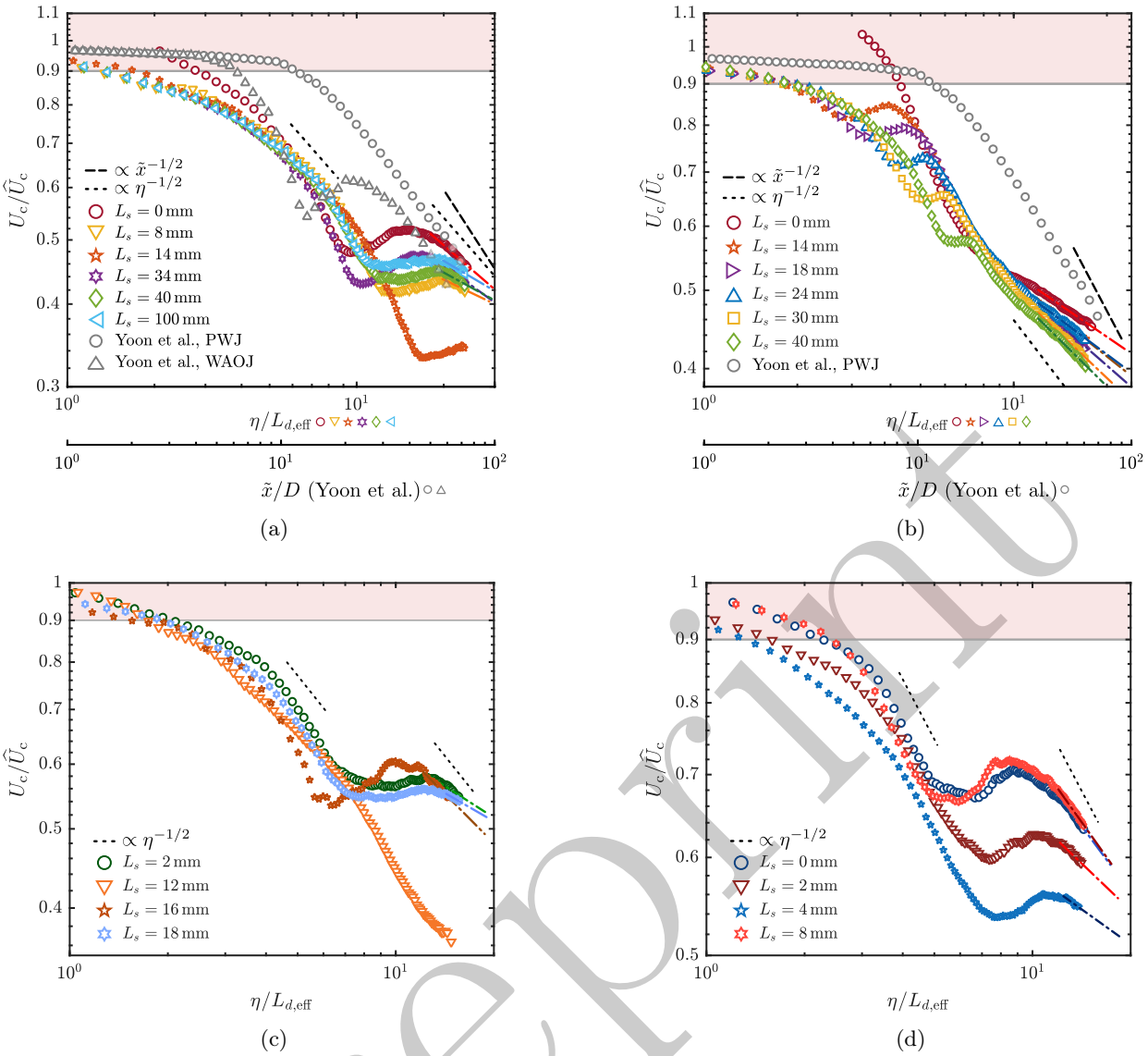

Fig. 10: **(a)** Normalized maximum velocity variation along the streamwise direction for the windshield-attached states with low primary duct angle shown in Fig. 8. **(b)** Dashboard-attached states (cf. Fig. 9). Data from Yoon et al. [77] of a plane wall jet (PWJ) and wall-attaching offset jet (WAOJ) is included for reference. **(c)** and **(d)** Windshield-attached states with increased primary duct angle (cf. Figs. B1a and B1b, respectively).

Table 6: Exponents of the power-law regression to the centerline velocity decay ζ and outer half-width growth χ for dashboard-attached states shown in Fig. 9.

L_s in mm	ζ	χ
0	-0.26	0.32
14	-0.30	0.43
18	-0.33	0.54
24	-0.29	0.65
28	-0.31	0.68
30	-0.35	0.68
40	-0.38	0.61

to $\eta/L_{d,\mathrm{eff}} \approx 15$ for $L_s = 14\,\mathrm{mm}$), outer growth rates decline with increasing dashboard distance, whereas the inner shear layers grow at similar sublinear rates irrespective of L_s or the primary duct angle β. An explanation for this behavior is the constraining effect of windshield proximity, which limits the shear layer development and attenuates its downstream growth. Growth rates in the outer half-width of the wall jet have not been determined under windshield-attached conditions because too few data points were available for regression, owing to the oblique jet exit angle relative to the boundaries of ROI 2.

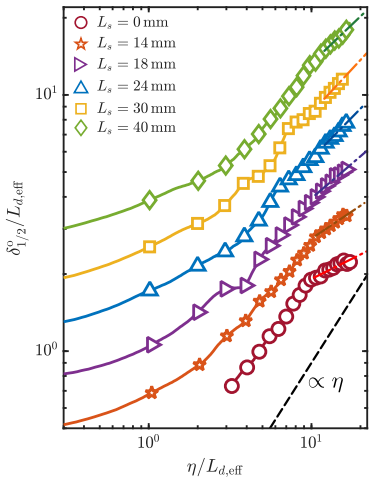

Fig. 11: Normalized outer half-width of the dashboard-attached states shown in Fig. 9. The curves are shifted for visibility by integer powers of 3/2 with respect to the lowest curve.

3.3 Statistical Analysis of Bistable State-Switching

Proper orthogonal decomposition (POD) was applied to the instantaneous PIV velocity fields to extract the modes associated with bistable state switching. Following the classical POD framework [83], the fluctuating velocity field, $\boldsymbol{U}'(\boldsymbol{x},t) = \boldsymbol{U}(\boldsymbol{x},t) - \langle \boldsymbol{U}(\boldsymbol{x}) \rangle$, is represented as a finite sum of orthonormal spatial modes and corresponding temporal coefficients,

$$\boldsymbol{U}'(\boldsymbol{x},t) = \sum_k a_k(t)\,\boldsymbol{\phi}_k(\boldsymbol{x}), \tag{7}$$

where $\boldsymbol{\phi}_k(\boldsymbol{x})$ denotes the k^{th} spatial mode and $a_k(t)$ its temporal coefficient. The modes are ordered according to their kinetic energy content, so that the leading modes describe the dominant large-scale flow features. Since in PIV applications the number of spatial degrees of freedom is typically much larger than the number of snapshots, the snapshot POD method of Sirovich [84] is commonly employed. In this approach, an $N \times N$ temporal correlation matrix $\mathbf{C}$ is formed from the ensemble of N fluctuating snapshots, with entries $C_{ij} = {}^1\!/_N \left(\boldsymbol{U}'(\boldsymbol{x},t_i), \boldsymbol{U}'(\boldsymbol{x},t_j)\right)$, where C_{ij} measures the inner-product (denoted by $(\cdot,\cdot)$) correlation between the snapshots at times t_i and t_j. The eigenvalue problem $\mathbf{C}\boldsymbol{v}^{(k)} = \lambda_k \boldsymbol{v}^{(k)}$ is then solved, where λ_k is the k^{th} eigenvalue and $\boldsymbol{v}^{(k)}$ is the corresponding eigenvector that provides the weights for reconstruction of the k^{th} POD mode from the snapshot ensemble. The associated temporal coefficients are obtained by projecting the fluctuating velocity fields onto the POD basis. In the present study, these temporal coefficients are used for the statistical characterization of bistable state switching.

Figure 12 summarizes the results of the statistical analysis applied to two ssw states at different duct angle and dashboard distance, respectively. Recall that these switching states are encountered at the boundaries of the monostable parameter range in Fig. 5a. Figure 12(a_1) shows the temporal coefficient $a_1^\star$ of the POD switching mode normalized by its respective RMS value for a duct angle of $\beta = 45.0°$ and dashboard position of $L_s = 32\,\mathrm{mm}$, plotted against dimensionless time $\tau = t/T$. On the right, the associated probability density function (PDF) is depicted. The average dwell time is defined as $T = {}^1\!/_N \sum_i^N \tilde{\Delta}_i$, where $\tilde{\Delta}_i$ denote individual residence intervals. A moving-average filter with a window size of 10 samples was applied to the time series and a threshold band of 30% of the minimum and maximum values was chosen to count single switching events. A clear bimodal separation is visible in the coefficient variation and PDF with a change of sign between state transitions, providing a suitable switching indicator. As an additional verification that the analysis captures the relevant switching dynamics and is not polluted by intra-state fluctuations, the eigenvalue spectra were compared to those of neighboring single-state configurations (not shown). In the quasi-steady cases, the leading mode contains only about 3–8% of the total fluctuation energy (depending on whether windshield or dashboard-attached flow is considered) and the energetic content is distributed over a large number of modes. In contrast, during bistable switching the energy of the leading mode increases to about 50%, which indicates that the dominant contribution stems from the global relocation of the jet between the two states.

For this parameter set, the jet alternates between complete windshield and dashboard attachment. Visual comparison with the instantaneous PIV snapshots in Fig. 12(a_4) links negative and positive coefficient values with the former and latter state, respectively. From the dwell times and PDF an asymmetry between both states is noticed that is also expressed within the time coefficient amplitudes. Since POD measures the distance from the global mean flow, the coefficient is biased towards the more frequently encountered windshield-attached flow.

The state switching appears to be random, with no distinct peaks identifiable in the power spectral density (PSD) estimate in Fig. 12(a_3). The PSD was calculated using Welch's method [85], as implemented in MATLAB's pwelch function, with the signal divided into two segments of 50% overlap and a rectangular window applied to each segment. The resemblance of the time coefficient variation to a random telegraph signal (RTS, black curve in Fig 12(a_1)) is reflected in the PSD in the form of a so-called Lorentzian spectrum. This characteristic shape is defined by a low-frequency plateau and a subsequent decay with a -2 slope at moderate to high frequencies. Figure 12(a_2) shows the associated dwell time survival function $P(\tau)$. This histogram represents the probability for individual dwell time intervals $\tilde{\Delta}_i$, i.e. the times between state-switching events, to be longer than time τ. Despite the few captured transitions, the correspondence with the exponential distribution $e^{-\tau}$ suggests a memoryless Poissonian process [86]. This means that the probability for a switching event to occur at any given moment is independent of the time already spend in the current state, which is consistent with random, noise-driven transitions [16].

An increased number of state transitions was found for a parameter set of $\beta = 55.9°$ and $L_s = 20\,\mathrm{mm}$, with the average dwell time decreasing to $T = 5\,\mathrm{s}$ compared to $T = 21.68\,\mathrm{s}$ in the previous case. For this configuration the jet changes between partial and full dashboard attachment. The more symmetrical PDF in Fig. 12(b_1) indicates that bias towards any state in unsteady configurations is sensitive to the precise parameter values. The state-switching regime likely occupies a finite band in parameter space, with small variations shifting the relative residence probability of both states. As the switching rate increases, the agreement with the exponential distribution in Fig. 12(b_2) improves significantly, thereby reinforcing the arguments presented earlier. The slight deviation in the high-frequency slope of the PSD from -2 can be explained by the finite transition time between states, compared to a theoretical RTS that does not experience inertia and relaxation.

In Fig. 12(a_1), an asymmetry is seen in the transition times between states, with the windshield-to-dashboard transition occurring rather rapidly compared to its counterpart. Figure 13 displays the switching mode together with the secondary mode extracted from the POD. This mode is interpreted as a measure for the relaxation dynamics within each state and is therefore referred to as the relaxation mode. The time coefficients in Fig. 13a reveal that the relaxation mode remains nearly inactive during the windshield phase, peaks during switching and enters an active phase during dashboard attachment. This pattern suggests a more stable attachment to the windshield with random bursts of dashboard attachment in between. The spatial structure of the relaxation mode in Fig. 13b shows that it extends over the region right above the dashboard, which indicates a gradual separation of the jet until transition towards the windshield.

4 Conclusions and Outlook

A generic, parameterized pseudo-2D defrost test rig was presented to investigate the occurrence of flow attachment associated with the Coandă effect in automotive windshield defrosting under conditions representative of passenger vehicles. Through systematic variation of the defrost duct angle and the distance between the duct exit and a simplified dashboard, parameter ranges associated with distinct jet-attachment regimes were identified, enabling the construction of a qualitative state map. Within this map, both quasi-steady configurations and unsteady configurations exhibiting stochastic switching between dashboard- and windshield-attached flow were observed. For low-to-moderate duct angles and moderate dashboard distances, a finite parameter range was identified in which only fully dashboard-attached flow was encountered. Furthermore, the experiments demonstrate that attachment to the windshield or the dashboard may persist for identical operating conditions over extended periods of time. Hence, bistability is confirmed as a physically relevant feature of automotive defroster flows.

A combination of pressure measurements on the windshield surface and particle image velocimetry provide a consistent physical characterization of the flow field. For windshield-attached flow at shallow duct angles, the measured pressure distributions display the characteristic signature of Coandă-dominated wall-attaching jets, including sub-atmospheric pressure upstream of attachment, a pronounced minimum and peak pressure in the stagnation region and subsequent pressure recovery in the wall-jet region. With increasing duct angle, the pressure field transitions toward a more impingement-dominated behavior. In all cases, the dashboard position was found to modify the pressure distribution substantially, shifting the location and magnitude of the pressure extrema and thereby altering the effective jet inclination and impingement strength at the windshield. Because the local Nusselt number distribution is reflected in the surface-pressure distribution, these effects are directly relevant to the windshield defrosting performance.

The mean velocity and turbulent kinetic energy fields confirm that dashboard proximity modifies the pre-attachment development of the jet and the subsequent wall-jet evolution in the near-field, thereby directly affecting the quality of windshield coverage. For windshield-attached flow, the centerline velocity decay depended on the dashboard position, with a deflection of the jet away from or towards the windshield being associated with a noticeably slower or faster decay, respectively. For dashboard-attached flow, the centerline velocity generally decayed more rapidly with increasing dashboard distance, while the outer half-width exhibited a stronger downstream growth, indicating enhanced jet spreading along the dashboard.

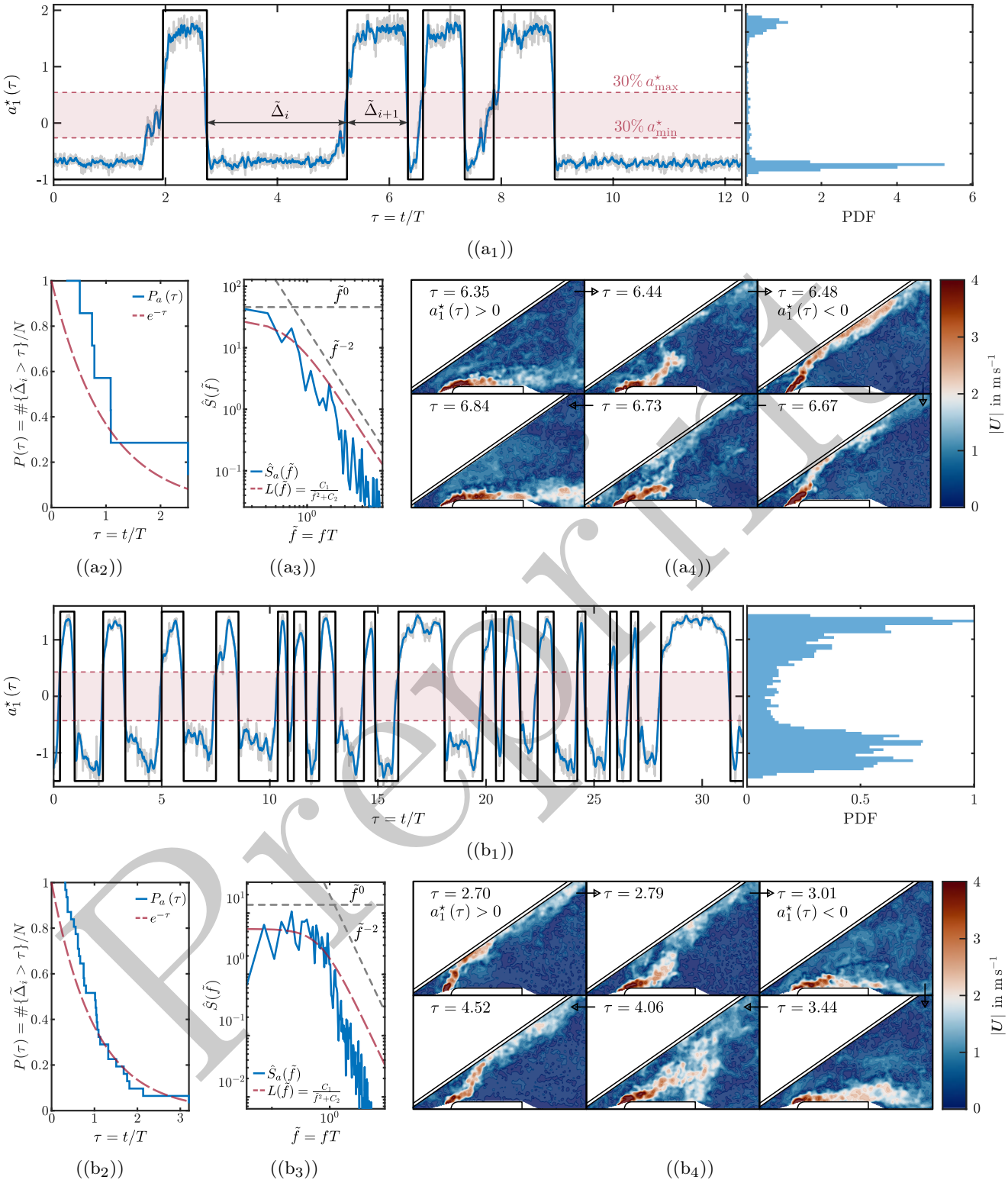

Fig. 12: Statistical analysis of random state switching occurring with **(a)** $\beta = 45.0°$, $L_s = 32\,\text{mm}$ and **(b)** $\beta = 55.9°$, $L_s = 20\,\text{mm}$. **$(\mathbf{a_1})|(\mathbf{b_1})$** Left: Normalized temporal coefficient of the dominant POD switching mode $a_1^\star$ (— moving average, — raw data). Right: Corresponding probability density function. **$(\mathbf{a_2})|(\mathbf{b_2})$** and **$(\mathbf{a_3})|(\mathbf{b_3})$**: Survival function P of dwell times $\tilde{\Delta}_i$ versus exponential distribution and corresponding power spectral density $\hat{S}$ of $a_1^\star$ with Lorentzian curve fit L ($C_1 = 10.26$, $C_2 = 0.36$ and $C_1 = 2.71$, $C_2 = 0.49$ in a_3 and b_3, respectively). **$(\mathbf{a_4})|(\mathbf{b_4})$**: Instantaneous velocity magnitude during state switching.

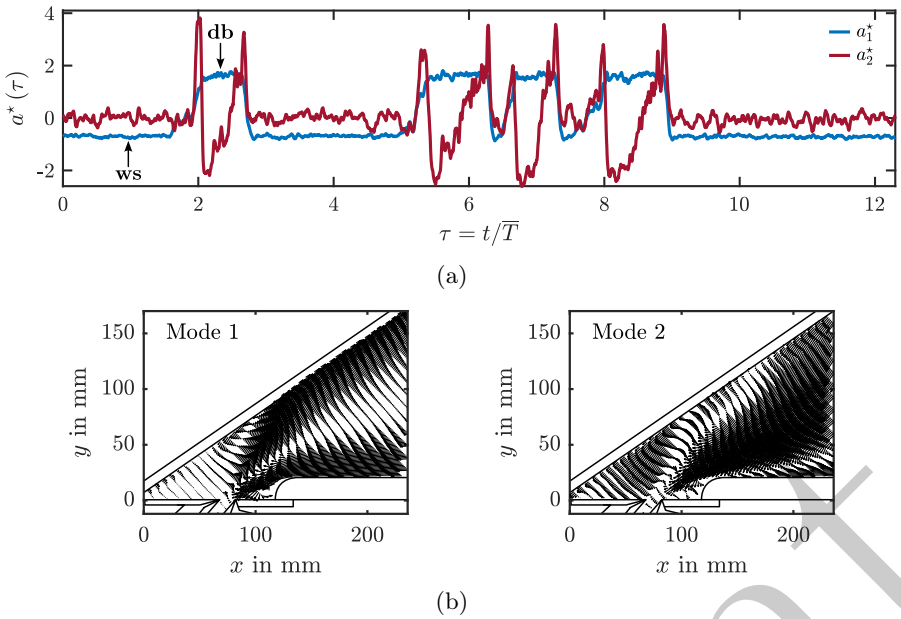

Fig. 13: **(a)** Normalized temporal coefficients of the first two dominant POD modes of random state-switching with $\beta = 45°$ and $L_s = 32\,\text{mm}$ (1: switching mode, 2: relaxation mode).**(b)** Corresponding eigenfunctions.

Proper orthogonal decomposition of the instantaneous PIV snapshots was used to extract the dominant switching dynamics in the unsteady parameter configurations. The leading mode captures the global relocation of the jet associated with transitions between dashboard- and windshield-attached flow, while the corresponding temporal coefficients reveal the stochastic nature of the switching events. The statistical analysis indicates that the switching process is consistent with approximately Poissonian behavior, supporting the interpretation of the observed dynamics as random transitions between coexisting attractors.

From an engineering standpoint, the results underline that the dashboard cannot be treated as a secondary detail in defroster design. In this respect, the present study provides a controlled experimental benchmark for future CFD validation, including a simplified yet representative geometry, well-defined inflow conditions and documented flow regimes. Potential for future investigations is seen in the influence of other key design factors, such as the dashboard geometry, windshield inclination angle and flow rate of the secondary jet. Furthermore, it remains to be determined whether the bistable jet attachment is coupled to the upstream flow development within the defrost duct, since existing findings indicate that such an interaction may be physically relevant.

The potential for bistable flow attachment has direct implications for the assessment of the predictive qualities of simulation methods used in the development process of modern defrosting systems. A detailed numerical study of the presented setup is therefore planned.

Acknowledgment

AS is grateful to his colleague Juan Londono Alfaro for fruitful discussions.

Funding Data

This research received no external funding.

Author Contributions

AS designed the study, developed the experimental setup, conducted the PIV experiments, analyzed the data and wrote the manuscript. TG developed the experimental setup, assisted with data acquisition and contributed to manuscript revision. AB supervised the work and contributed to manuscript revision. All authors approved the final manuscript.

Conflict of Interest

AS and TG were employed by the company Volkswagen AG. AB declares that the research was conducted in the absence of any commercial or financial relationships that could be construed as a potential conflict of interest. The results, opinions and conclusions of this study are not necessarily those of Volkswagen AG.

Data Availability Statement

The data presented in this study are available upon reasonable request from the corresponding author due to the Volkswagen AG individual data disclosure approval process.

A Flow Field Topology of Dashboard-Attached States

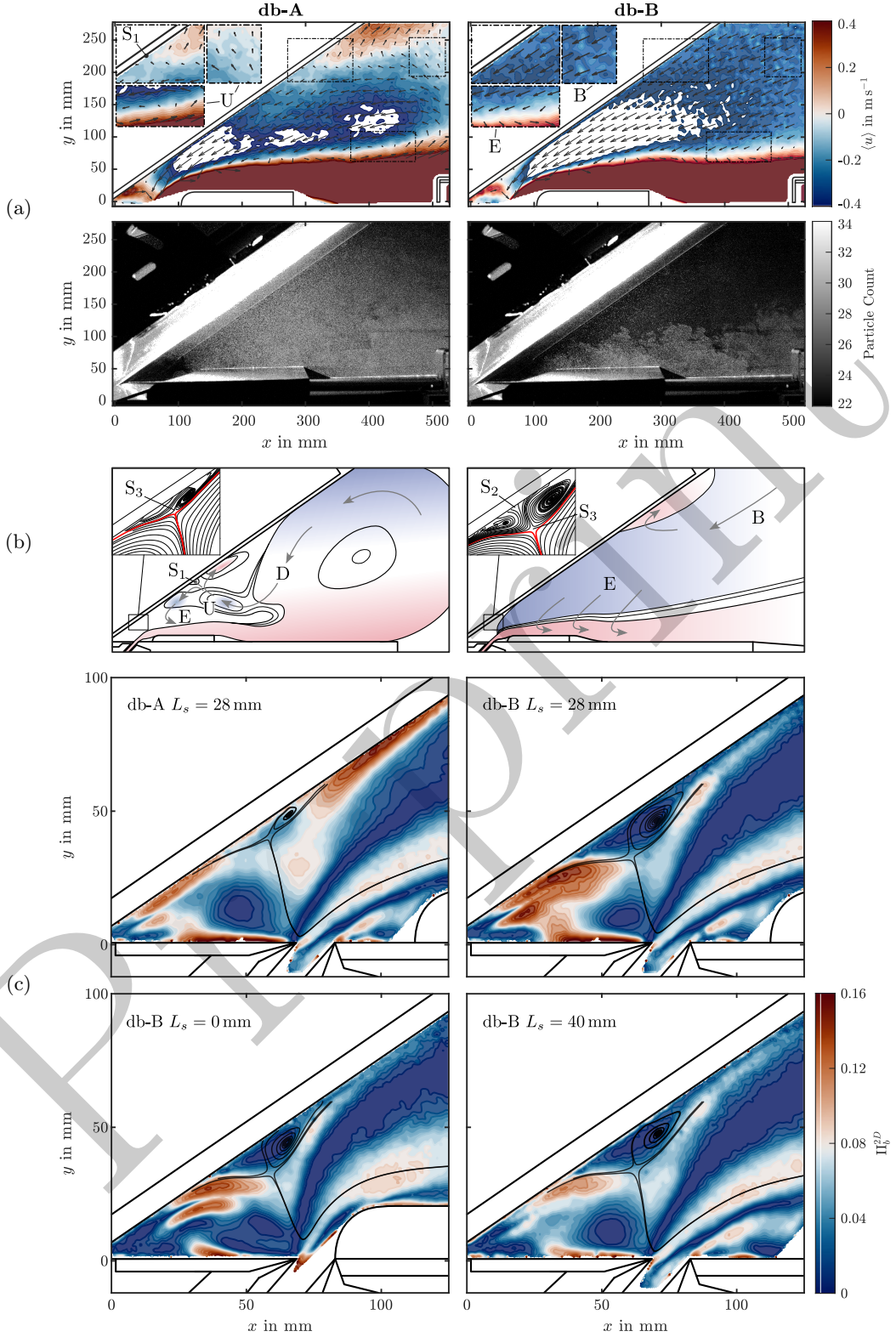

Fig. A1: **(a)** Mean velocity component $\langle u \rangle$ with $\beta = 45.0°$ and $L_s = 24\,\text{mm}$, averaged over 100 PIV samples indicating the existence of a large-scale vortical structure downstream of the dashboard in case of state db-A, resulting in an area wide redistribution of tracers within the measurement plane. **(b)** Schematic depiction of the global flow topology and detailed view of local streamline distribution in the lower region of the windshield. B: Backflow, D: Downwash, E: Entrainment, S_1 | S_2: Stagnation point, S_3: Saddle point, U: Upwash. **(c)** Contours of the second invariant of the anisotropy tensor near the windshield base.

Examination of the seeding particle distribution during the experiments provided an initial indication of the occurrence of two distinct dashboard states within the region of spontaneous dashboard attachment in the state map (cf. 5a), referred to as monostable region. Figure A1a depicts this situation exemplarily for $L_s = 24\,\mathrm{mm}$ and $\beta = 45°$. For db-B, the intermittent jet boundary contrasts sharply against the tracer-poor background, which is not the case for db-A due to the widespread redistribution of DEHS particles. Since the laboratory ventilation system counteracts the continuous accumulation of DEHS in the room and the particle image may vary randomly between the two states, the particles can only originate from the jet itself. In case of db-A, contours of the time-averaged streamwise velocity component reveal the existence of a stagnation point (S_1) on the windshield surface, where the backflow diverges and is partially deflected in the positive x-direction. This stagnation point is caused by an upwash zone (U), noticeable just within the bounds of ROI 1. Contrary to this, no such features are present for db-B and the backflow (B) is oriented approximately parallel to the windshield (as evident from the vector directions). Such a flow topology is likely produced by a large-scale vortical structure located downstream of the ROI chosen for our experiments (cf. A1b) , the exact structure of which can therefore only be hypothesized. The recirculated air separates from the windshield surface (D), thereby leading to the formation of (U) and (S_1) as air is flowing in to balance the corresponding low pressure. Part of the flow diverging from (S_1) in negative x-direction is then entrained again into the jet. In contrast, the backflow for db-B originates from ambient air beyond the windshield and therefore exhibits a significantly lower particle density. The Coandă jet is not redirected and leaves the visible area without coming into contact with the windshield.

A second separation zone is found from the PIV results in the area near the windshield base, as indicated by the streamlines in Fig. A1b. Where the backflow collides with the secondary jet, a saddle point (S_3) is formed at the outermost point of the separation zone, which in the case of db-B encloses a pair of counter-rotating vortices, accompanied by the development of another stagnation point (S_2). For db-A, this zone is less pronounced, so that (S_3) is shifted closer to the windshield and no stagnation point is present including only a single identifiable vortex.

The more distinct recirculation zone is associated with earlier separation of a less energetic backflow from the surface of the windshield in the case of state db-B. This observation together with the pronounced stagnation point (S_2) suggests an increased pressure in that region compared to db-A and therefore a stronger negative pressure gradient from the windshield toward the dashboard, which is more capable of sustaining the Coandă effect across parameter changes that lie outside of the monostable region. Figure A1c shows contours of the second invariant of the anisotropy tensor, defined as:

$$\mathrm{II}_b^{2D} = b_{ij}b_{ji}, \quad \text{with } b_{ij} = \frac{\langle u_i' u_j' \rangle}{2k} - \frac{1}{3}\delta_{ij}.$$

Here, u_i' denotes the fluctuating velocity component along direction i, b_{ij} is the deviatoric part of the Reynolds-stress tensor normalized with the turbulent kinetic energy k and δ_{ij} is the Kronecker delta. The quantity II_b^{2D} provides a measure of the magnitude of anisotropic turbulent stresses irrespective of coordinate-frame orientation and is used here to emphasize differences in the local flow topology near the windshield base area between db-A and db-B. It is evident that the structure of the dashboard-attached flow in the case of parameter configurations outside the monostable range ($L_s = 0\,\mathrm{mm}$ and $L_s = 40\,\mathrm{mm}$) corresponds to that of the state defined as db-B. Besides the clearly recognizable separation zone of db-B, a local increase in turbulent shear intensity is noticed above the merging point of the primary and secondary jets in case of db-A. With the saddle point (S_3) shifted upwards compared to db-B, the more pronounced parallel alignment of the secondary jet and stronger backflow cause the turbulent momentum transport to become increasingly directional. Outside of the monostable region, this pattern has not been found, which coincides with the observation that db-A is unstable for these parameter configurations, as described in Sec. 3.1.

Although two-dimensionality of the flow field was assessed by spanwise displacement of the laser sheet during the experimental investigations in this study (cf. supp. Sec. 3), a definitive statement about the global three-dimensional structure of the flow at any given time during the occurrence of the two dashboard states is beyond the capabilities of 2D2C PIV. This makes it impossible to unambiguously determine the underlying cause of the observed behavior. Nevertheless, we would like to outline a possible scenario at this point.

We assume that the flow essentially remains attached to the dashboard across the entire span for db-B, but becomes three-dimensional for db-A, with part of the jet being attached to the dashboard near mid-span, but regions of windshield attachment occurring closer to one or both side walls. In this case, reduced pressure in the area enclosed by the primary jet and the windshield would cause air from nearby dashboard-attached flow to be deflected towards the windshield and drawn into the low-pressure region, thereby leading to the saturation with tracer particles within the ROI. As the partially windshield-attached flow may not be stable over time, stochastic perturbations in the flow would trigger occasional attachment to the dashboard, in correspondence with the random transitions between db-A and db-B. Indications of this might be reflected in the asymmetric flow pattern found during the two-dimensionality assessment shown in Fig. 11b of the supplementary material,

where the jet exhibits noticeably weak dashboard-attachment at the location $z = -250\,\mathrm{mm}$. However, since the individual spanwise positions were examined in sequence, it is not possible to draw any conclusions regarding the influence this has on the flow in the center plane.

B Mean Velocity and Turbulent Kinetic Energy Contours for $\beta = 61.9°$ and $\beta = 80.6°$

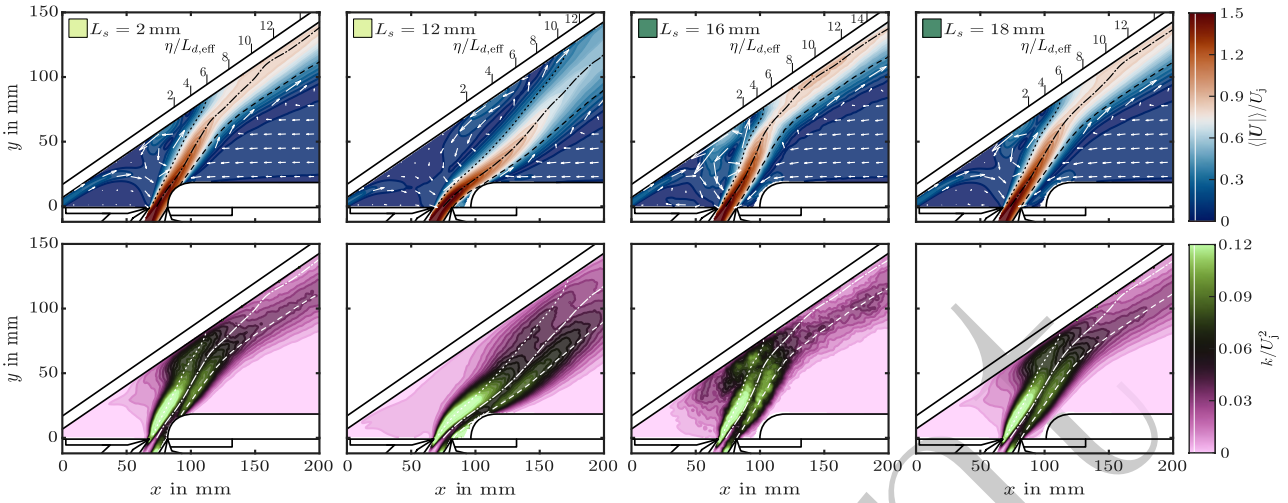

(a) $\beta = 61.9°$

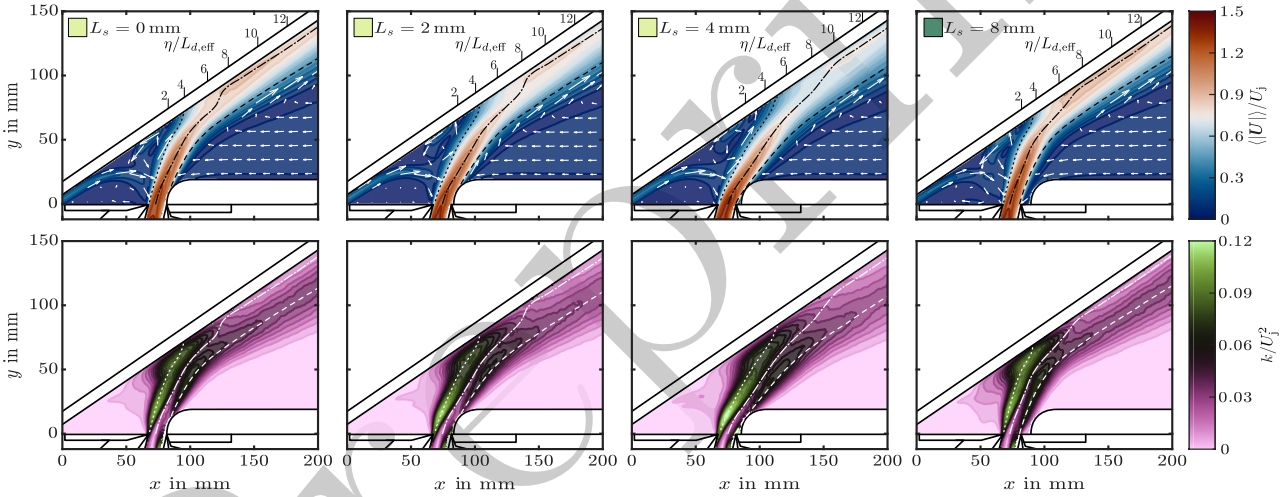

(b) $\beta = 80.6°$

Fig. B1: Normalized time-averaged velocity magnitude (top rows) and turbulent kinetic energy fields for windshield-attached states with increased primary duct angle. --- Inner half-width. -- Outer half-width. --- Primary jet centerline.

C Jet Cross-Stream Profiles of Mean Velocity and Second-Order Turbulence Statistics

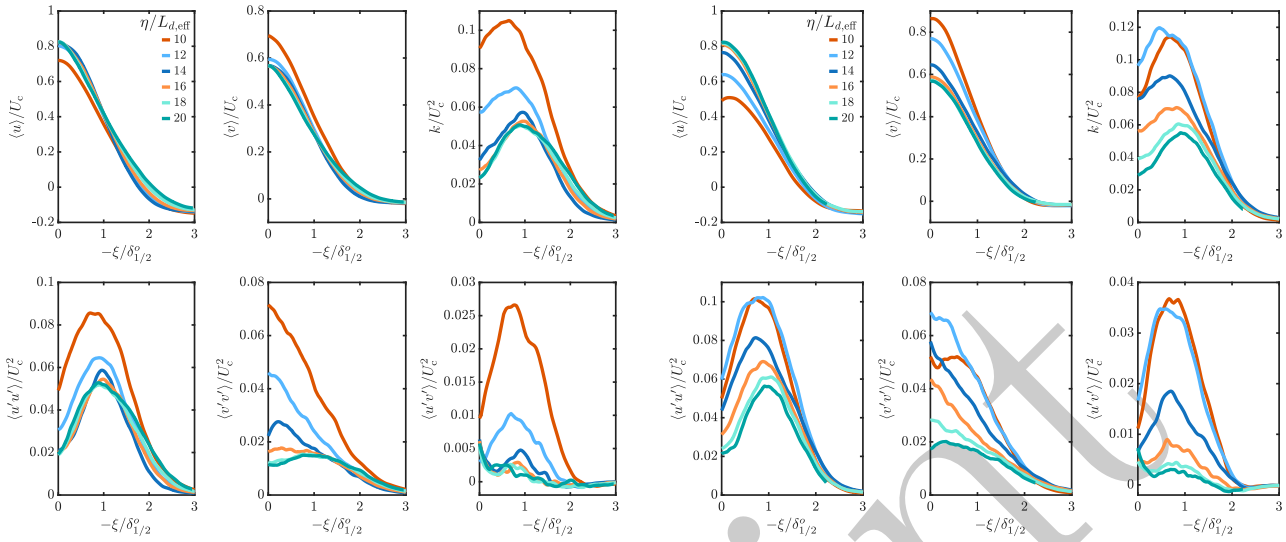

(a) $L_s = 0\,\mathrm{mm}$.

(b) $L_s = 8\,\mathrm{mm}$.

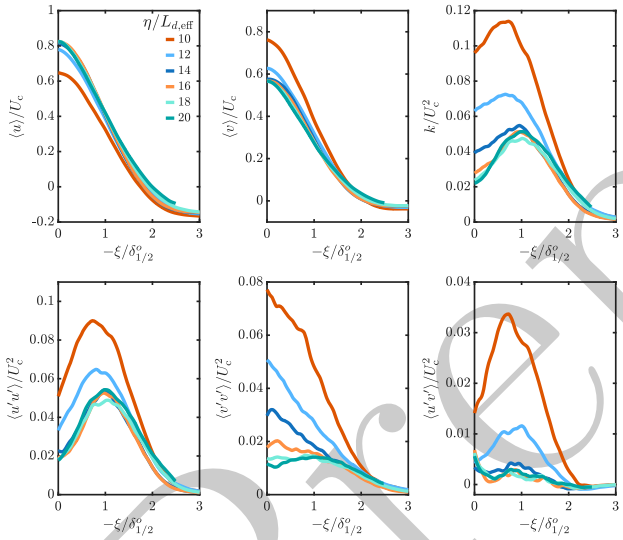

(c) $L_s = 34\,\mathrm{mm}$.

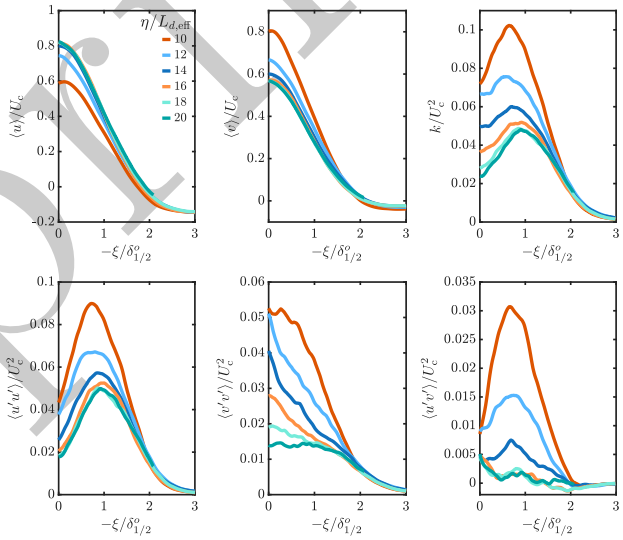

(d) $L_s = 100\,\mathrm{mm}$.

Fig. C1: Normalized first- and second-order velocity field statistics in the outer layer of windshield-attached states with $\beta = 45°$.

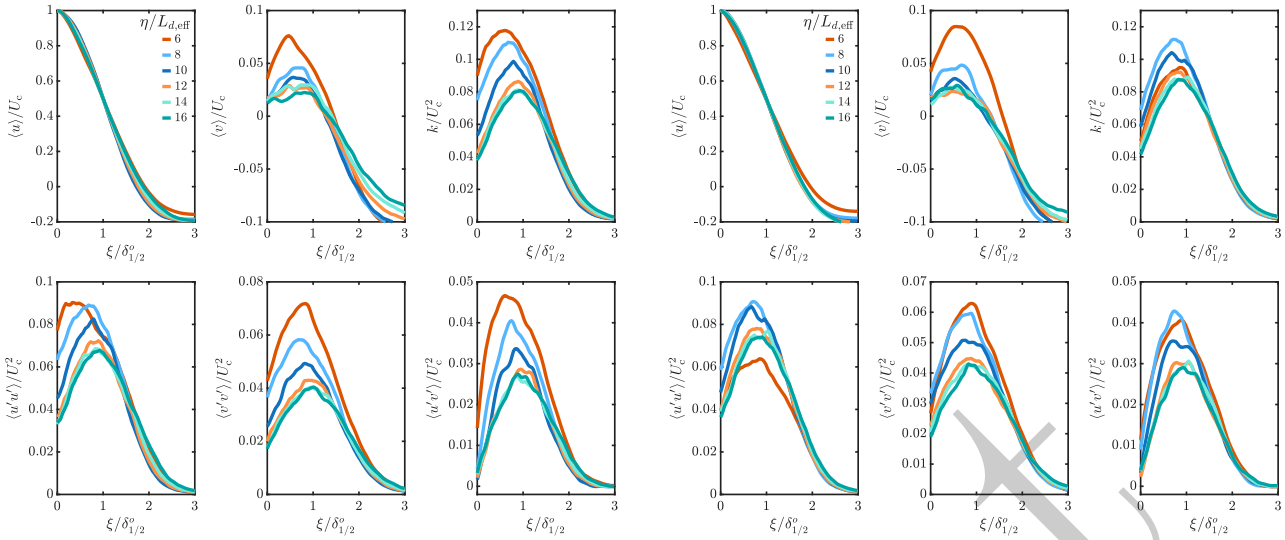

(a) $L_s = 0\,\mathrm{mm}$.

(b) $L_s = 14\,\mathrm{mm}$.

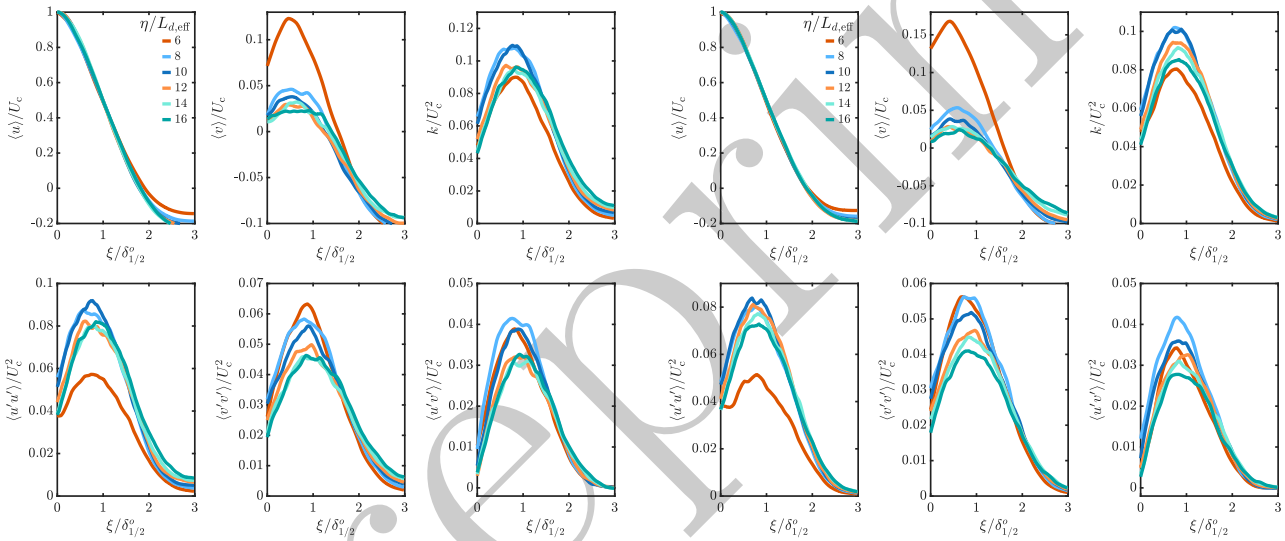

(c) $L_s = 18\,\mathrm{mm}$.

(d) $L_s = 24\,\mathrm{mm}$.

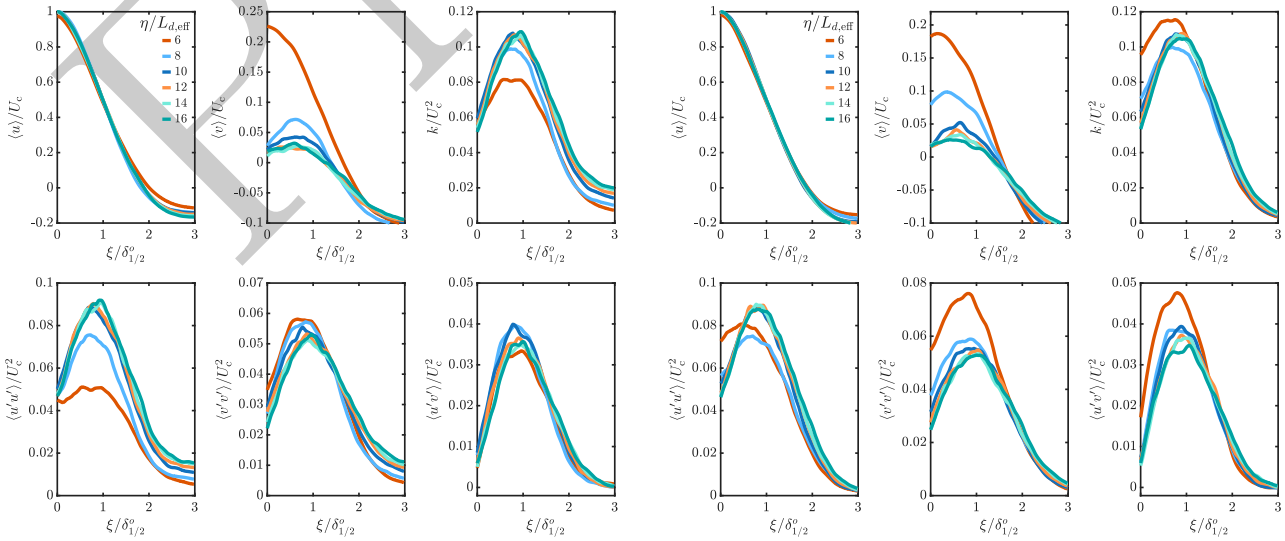

(e) $L_s = 30\,\mathrm{mm}$.

(f) $L_s = 40\,\mathrm{mm}$.

Fig. C2: Normalized first- and second-order velocity field statistics in the outer layer of dashboard-attached states with $\beta = 45°$.

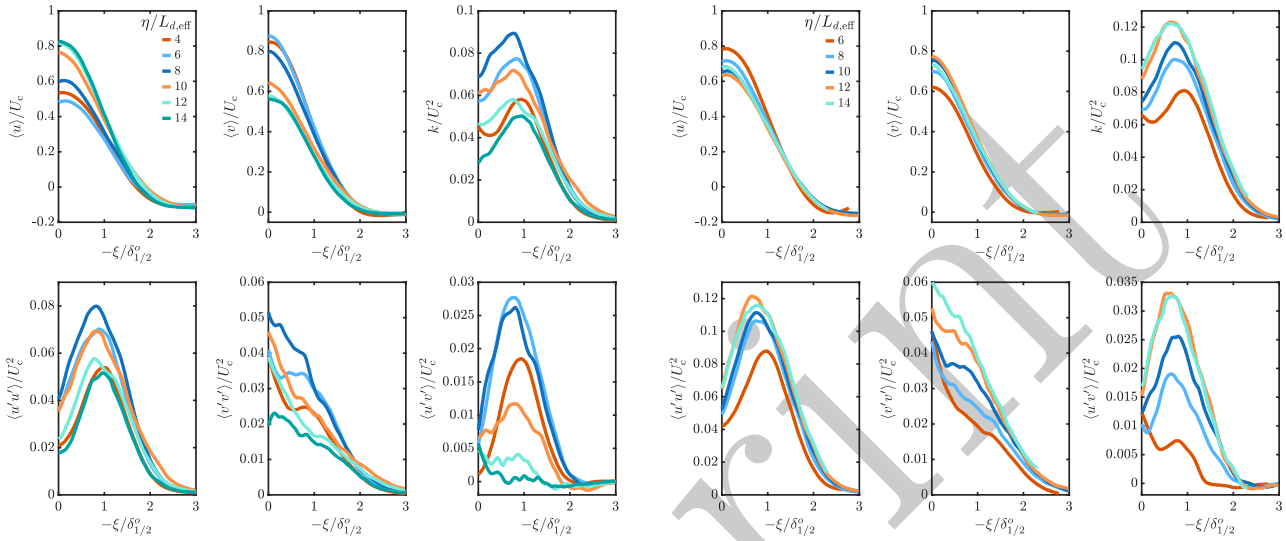

(a) $L_s = 2\,\mathrm{mm}$.

(b) $L_s = 12\,\mathrm{mm}$.

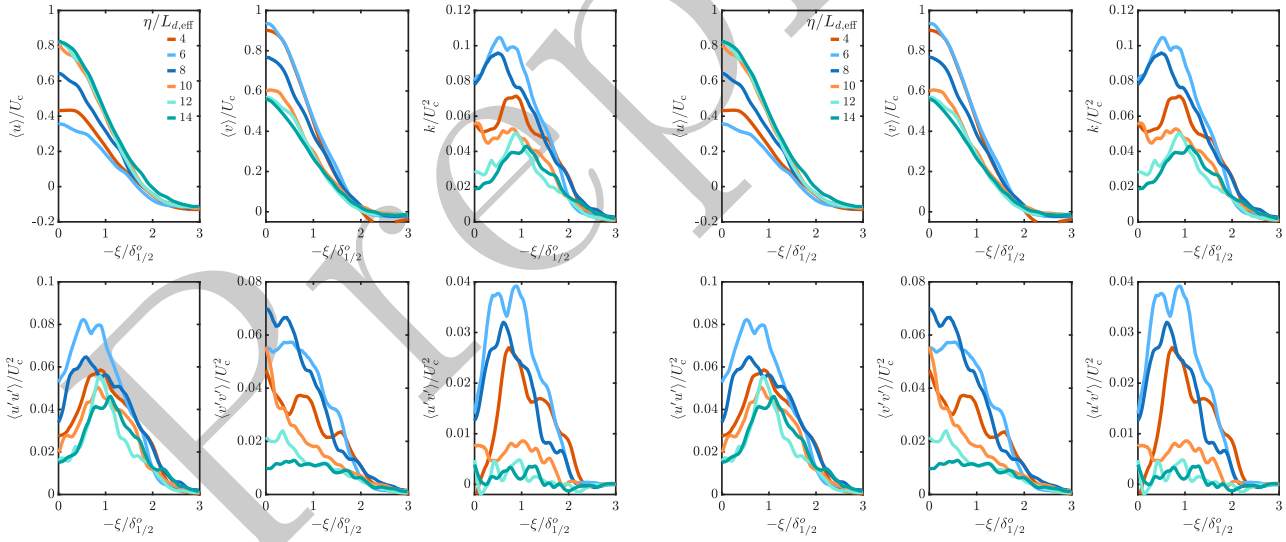

(c) $L_s = 16\,\mathrm{mm}$.

(d) $L_s = 18\,\mathrm{mm}$.

Fig. C3: Normalized first- and second-order velocity field statistics in the outer layer of windshield-attached states with $\beta = 61.9°$.

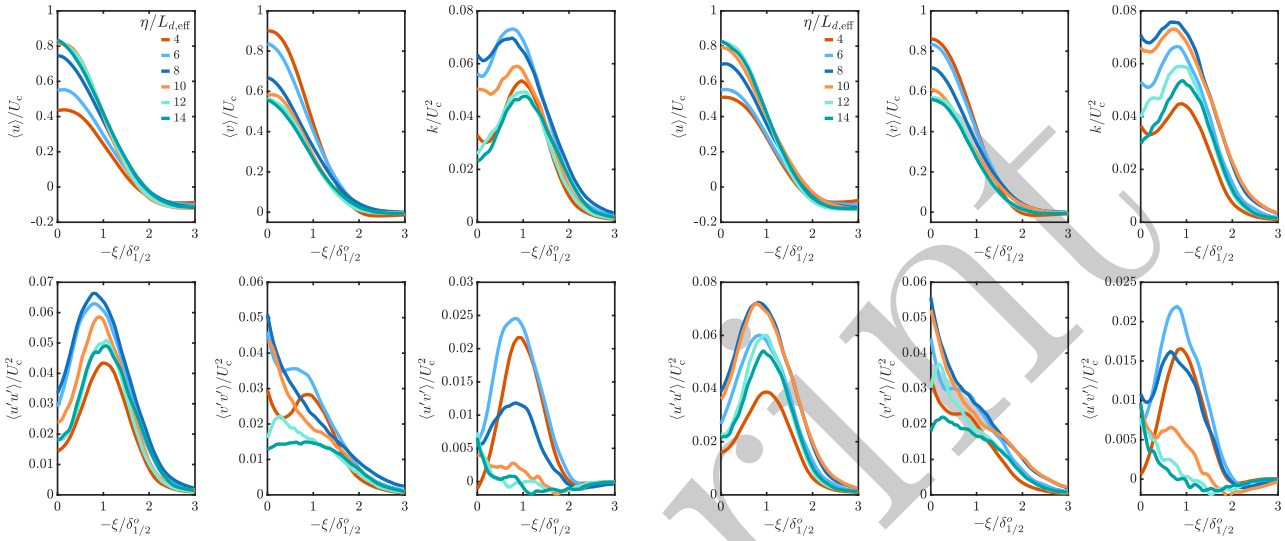

(a) $L_s = 0\,\mathrm{mm}$.

(b) $L_s = 2\,\mathrm{mm}$.

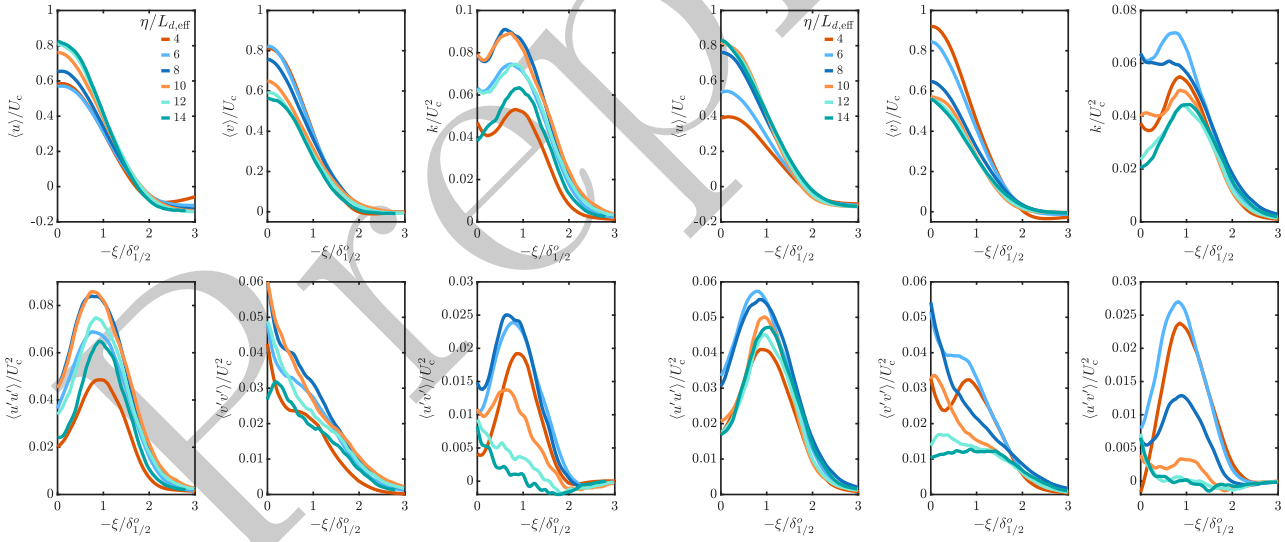

(c) $L_s = 4\,\mathrm{mm}$.

(d) $L_s = 8\,\mathrm{mm}$.

Fig. C4: Normalized first- and second-order velocity field statistics in the outer layer of windshield-attached states with $\beta = 80.6°$.

D Outer and Inner Half-Width for Windshield-Attached States

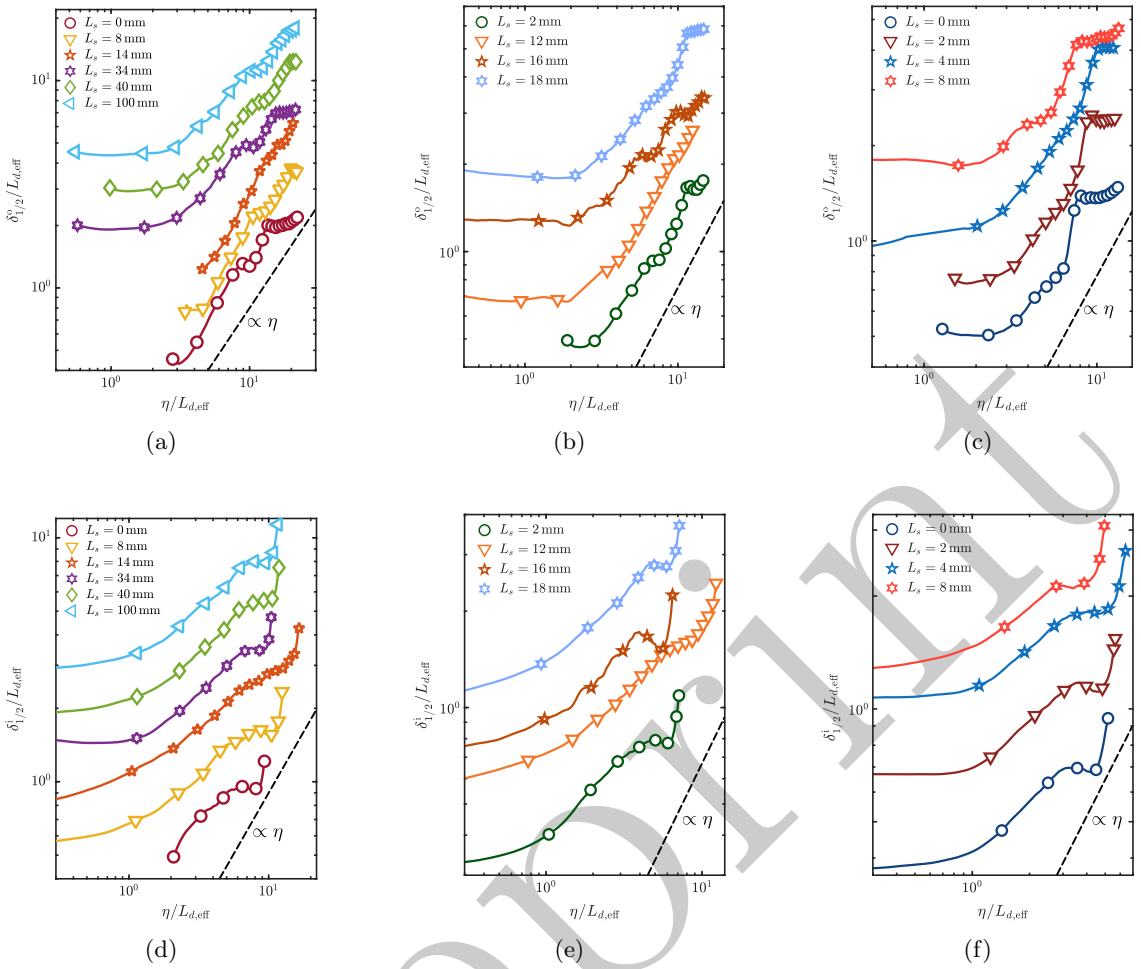

Fig. D1: **(a)** Normalized outer half-width of the windshield-attached states shown in Fig. 8. **(b)** and **(c)** Increased primary duct angle (cf. Fig. B1a and B1b, respectively). **(d)-(f)** Inner half-width (free jet region) (same cases as (a)-(c)). The curves are shifted for visibility by integer powers of $3/2$ with respect to the lowest curve.

References

[1] European Parliament: Regulation (EU) 2019/2144 of the European Parliament and of the Council of 27 November 2019 on type-approval requirements for motor vehicles and their trailers, and systems, components and separate technical units intended for such vehicles, as regards their general safety and the protection of vehicle occupants and vulnerable road users. https://eur-lex.europa.eu/legal-content/EN/TXT/?uri=CELEX%3A02019R2144-20250901 (2019)

[2] Young, T.: Vii. outlines of experiments and inquiries respecting sound and light. Philosophical Transactions of the Royal Society of London (90), 106–150 (1800) https://doi.org/10.1098/rstl.1800.0008 https://royalsocietypublishing.org/rstl/article-pdf/doi/10.1098/rstl.1800.0008/1463307/rstl.1800.0008.pdf

[3] T. López-Arias: Could the Coandă effect be called the Young effect? The understanding of fluid dynamics of a legendary polymath. European Journal of Physics **33**(2), 253–263 (2012) https://doi.org/10.1088/0143-0807/33/2/253 arXiv:1103.6097 [physics.hist-ph]

[4] Coandă, H.M.: Device for deflecting a stream of elastic fluid projected into an elastic fluid. https://patents.google.com/patent/US2052869A/en (1936)

[5] Coandă, H.M.: Lifting apparatus. https://patents.google.com/patent/US3261162A/en (1964)

[6] Wang, S., Batikh, A., Baldas, L., Kourta, A., Mazellier, N., Colin, S., Orieux, S.: On the modelling of the switching mechanisms of a coanda fluidic oscillator. Sensors and Actuators A: Physical **299**, 111618 (2019) https://doi.org/10.1016/j.sna.2019.111618

[7] Xu, K., Su, X., Bensow, R., Krajnovic, S.: Drag reduction of ship airflow using steady coanda effect. Ocean Engineering **266**, 113051 (2022) https://doi.org/10.1016/j.oceaneng.2022.113051

[8] Tanveer, A., Ahmad, S.M.: Exploration of fluidic thrust vectoring control on a dynamic test rig: Computational and experimental analysis. Engineering Proceedings **56**(1) (2023) https://doi.org/10.3390/ASEC2023-15315

[9] Arai, M., Amagai, K., Ebara, T.: Attitude Control of a Diesel Spray Under the Coanda Effect. In: International Fuels & Lubricants Meeting & Exposition (1994). https://doi.org/10.4271/941923 . https://legacy.sae.org/publications/technical-papers/content/941923/

[10] Skotnicka-Siepsiak, A.: The applicability of coanda effect hysteresis for designing unsteady ventilation systems. Energies **14**(1) (2021) https://doi.org/10.3390/en14010034

[11] Pitton, G., Quaini, A., Rozza, G.: Computational reduction strategies for the detection of steady bifurcations in incompressible fluid-dynamics: Applications to coanda effect in cardiology. Journal of Computational Physics **344**, 534–557 (2017) https://doi.org/10.1016/j.jcp.2017.05.010

[12] Walker, M.A., Pinier, J.T., Shea, P.R., Collins, J.G., Mears, L., Lee, M.W., Pomeroy, B.W.: Experimental Identification of Bistable Flow States on the Space Launch System at Liftoff Conditions. American Institute of Aeronautics and Astronautics, ??? (2022). https://doi.org/10.2514/6.2022-3665 . https://arc.aiaa.org/doi/abs/10.2514/6.2022-3665

[13] Shi, N.-X., Gu, Y.-S., Zhou, Y.-H., Wang, L.-X., Feng, C., Li, L.-K.: Mechanism of hysteresis and uncontrolled deflection in jet vectoring control based on coanda effect. Physics of Fluids **34**(8), 084107 (2022) https://doi.org/10.1063/5.0101994 https://pubs.aip.org/aip/pof/article-pdf/doi/10.1063/5.0101994/16579027/084107$_1$$_o$*nline.pdf*

[14] Vanierschot, M., Van den Bulck, E.: Hysteresis in flow patterns in annular swirling jets. Experimental Thermal and Fluid Science **31**(6), 513–524 (2007) https://doi.org/10.1016/j.expthermflusci.2006.06.001

[15] Trávníček, Z., Tesař, V.: Hysteresis in annular impinging jets. Experimental Thermal and Fluid Science **44**, 565–570 (2013) https://doi.org/10.1016/j.expthermflusci.2012.08.019

[16] Cicolin, M.M., Bearman, P.W., Assi, G.R.S., Buxton, O.R.H.: Bistability in the wake of a circular cylinder with passive control using two leeward rods. Journal of Fluids and Structures **120**, 103918 (2023) https://doi.org/10.1016/j.jfluidstructs.2023.103918

[17] Mears, L., Shea, P.R., Collins, J.G., Pinier, J.T., Gildersleeve, S., Eppink, J.L., Bartram, S., Jenkins, L., Yao, C.-S., Burnette, D.: Asymmetric Flow State Switching in the Space Launch System Block 2 Liftoff Environment. American Institute of Aeronautics and Astronautics, ??? (20224). https://doi.org/10.2514/6.2024-0466 . https://arc.aiaa.org/doi/abs/10.2514/6.2024-0466

[18] Newman, B.G.: The deflexion of plane jets by adjacent boundaries - coanda effect. In: Boundary Layer and Flow Control vol. 1, pp. 232–264. G. V. Lachmann, ??? (1960)

[19] Bourque, C., Newman, B.G.: Reattachment of a two-dimensional, incompressible jet to an adjacent flat plate. The Aeronautical Quarterly **11**, 201–232 (1960)

[20] Allery, C., Guerin, S., Hamdouni, A., Sakout, A.: Experimental and numerical pod study of the coanda effect used to reduce self-sustained tones. Mechanics Research Communications **31**(1), 105–120 (2004) https://doi.org/10.1016/j.mechrescom.2003.08.003

[21] Skotnicka-Siepsiak, A.: Hysteresis of the coanda effect. Journal of Fluids Engineering **140**(1), 011202 (2017) https://doi.org/10.1115/1.4037522 https://asmedigitalcollection.asme.org/fluidsengineering/article-pdf/140/1/011202/6201222/fe$_1$40$_0$1$_0$11202.*pdf*

[22] Aroussi, A., Hassan, A., Clayton, B., AbdulNour, B.S., Rice, E.: Comparison of Performance Between Several Vehicle Windshield Defrosting and Demisting Mechanisms. In: SAE 2000 World Congress

(2001). https://doi.org/10.4271/2000-01-1278 . https://www.sae.org/papers/improving-vehicle-windshield-defrosting-demisting-2000-01-1278

[23] Aroussi, A., Hassan, A., Clayton, B., AbdulNour, B.S.: Comparison of Performance Between Several Vehicle Windshield Defrosting and Demisting Mechanisms. In: SAE 2001 World Congress (2001). https://doi.org/10.4271/2001-01-0582 . https://legacy.sae.org/publications/technical-papers/content/2001-01-0582/

[24] Aroussi, A., Hassan, A., Morsi, Y.: Numerical simulation of the airflow over and heat transfer through a vehicle windshield defrosting and demisting system. Heat and Mass Transfer **39**(5), 401–405 (2003) https://doi.org/10.1007/s00231-002-0307-x

[25] Rasipuram, S., Nasr, K.: A Parametric Computationally - Based Study of Windshield Heat Transfer Subject to Impinging Airflow. In: SAE 2004 World Congress & Exhibition (2004). https://doi.org/10.4271/2004-01-1382 . https://www.sae.org/papers/a-parametric-computationally-based-study-windshield-heat-transfer-subject-impinging-airflow-2004-01-1382

[26] Mattiello, F., Croce, G., Angelis, A.D.: CFD Methodology to Predict Demisting Phenomena on the Car Windows. Engineering Systems Design and Analysis, vol. Volume 4: Fatigue and Fracture, Heat Transfer, Internal Combustion Engines, Manufacturing, and Technology and Society, pp. 281–287 (2006). https://doi.org/10.1115/ESDA2006-95398 . American Society of Mechanical Engineers. https://doi.org/10.1115/ESDA2006-95398

[27] Kang, S.J., Kader, M.F., Jun, Y.D., Lee, K.B.: Automobile defrosting system analysis through a full-scale model. International Journal of Automotive Technology **12**(1), 39–44 (2011) https://doi.org/10.1007/s12239-011-0005-0

[28] Kumar, M.A., Kanniah, K.: Computational Investigation for Flow and Heat Transfer Characteristics of Automobile Windshield with Impinging Slot Jets. In: SAE 2012 World Congress & Exhibition (2004). https://doi.org/10.4271/2012-01-1219 . https://www.sae.org/papers/computational-investigation-flow-heat-transfer-characteristics-automobile-windshield-impinging-slot-jets-2012-01-1219

[29] Goldasteh, I., Chang, S., Maaita, S., Mathur, G.: Numerical Simulation of Airflow Distribution on the Automobile Windshield in Defrost Mode. In: SAE 2015 World Congress & Exhibition (2015). https://doi.org/10.4271/2015-01-0330 . https://www.sae.org/papers/numerical-simulation-airflow-distribution-automobile-windshield-defrost-mode-2015-01-0330

[30] He, Z., Qu, X., Ji, L., Wu, W., Wang, X.: Analysis and optimization of truck windshield defroster. Applied Sciences **10**(16) (2020) https://doi.org/10.3390/app10165671

[31] Kim, D., Lee, J.W., Song, R., Gim, Y., Kwon, H., Ko, H.S., Lee, J.: Improvement of defogging performance of automobile defroster using vortex generators. Heat and Mass Transfer **56**(8), 2595–2604 (2020) https://doi.org/10.1007/s00231-020-02879-w

[32] Özcan, O., Yildiz, A., Coskun, A.: An approximation and cfd validation in dashboard nozzles for reviewing demisting and deicing issues in windshields. Automotive Technical Papers (2022) https://doi.org/10.4271/2022-01-5035

[33] Sakamoto, H., Watanabe, T., Taniguchi, F.: An analysis of frost formation on vehicle windows. SAE 1987 Transactions (1987) https://doi.org/10.4271/870028

[34] Ikeda, Y., Katoh, N., Ishii, N., Kuriyama, T.: Numerical analysis of the airflow on windows from defroster nozzles (in japanese). JSAE paper **924076** (1992)

[35] Sugano, M., Yamada, T., Takesue, Y., Yasuk, T.: Numerical analysis of defroster cleaning pattern: Prediction of the airflow near the windshield glass using three-dimensional analysis (in japanese). JSAE Review **15**(3), 269 (1994)

[36] AbdulNour, B.S.: Hot-wire velocity measurements of defroster and windshield flow. SAE 1997 Transactions - Journal of Passenger Cars (1997) https://doi.org/10.4271/970109

[37] AbdulNour, B.S.: Numerical simulation of vehicle defroster flow field. SAE 1998 Transactions - Journal of Passenger Cars **107**(6) (1998) https://doi.org/10.4271/980285

[38] AbdulNour, B.S.: CFD Prediction of Automotive Windshield Defrost Pattern. In: SAE International

Congress & Exposition (1999). https://doi.org/10.4271/1999-01-1203 . https://www.sae.org/papers/cfd-prediction-automotive-windshield-defrost-pattern-1999-01-1203

[39] Skea, A., Harrison, R., Baxendale, A., Fletcher, D.: Comparison of CFD Simulation Methods and Thermal Imaging with Windscreen Defrost Pattern. In: SAE Vehicle Thermal Management Systems Conference & Exposition (2001). https://doi.org/10.4271/2001-01-1720 . https://www.sae.org/papers/comparison-cfd-simulation-methods-thermal-imaging-windscreen-defrost-pattern-2001-01-1720

[40] Becker, S., Lienhart, H., Stoots, C., Beier, M., Hofhaus, J., Schlenz, D., Zemsch, S., Ryssel, E.: Investigations of automotive defroster and windshield flow. In: ATTCE 2001 Proceedings, vol. 2, pp. 368–391 (2001). https://doi.org/10.4271/2001-01-3441 . https://legacy.sae.org/publications/technical-papers/content/2001-01-3441/

[41] Roy, S., Nasr, K., Patel, P., AbdulNour, B.: An experimental and numerical study of heat transfer off an inclined surface subject to an impinging airflow. International Journal of Heat and Mass Transfer **45**(8), 1615–1629 (2002) https://doi.org/10.1016/S0017-9310(01)00276-9

[42] Kang, S.-H., Lee, J.-H., Byun, J.-S.: 3d unsteady numerical analysis to design defrosting system of automotive windshield glass (in korean). Transactions of the Korean Society of Automotive Engineers **15**(5), 1–8 (2007)

[43] Nasr, K.J., Abdulnour, B.S.: Defrosting of automotive windshields: progress and challenges. International Journal of Vehicle Design **24**, 360–375 (2000)

[44] Patidar, A.: Comparison of CFD Analysis Methods for Simulating De-Icing Pattern over Automotive Windshield and Windows. In: SAE 2010 World Congress & Exhibition (2010). https://doi.org/10.4271/2010-01-0555 . https://www.sae.org/papers/comparison-cfd-analysis-methods-simulating-de-icing-pattern-automotive-windshield-windows-2010-01-0555

[45] Sen, S., Selokar, M., Nisad, D., Kishore, K.: Design and Development of Demisting Device of a Commercial Vehicle and Its Numerical as Well as Experimental Validation. In: SAE 2016 World Congress and Exhibition (2016). https://doi.org/10.4271/2016-01-0217 . https://www.sae.org/papers/design-development-demisting-device-a-commercial-vehicle-numerical-well-experimental-validation-2016-01-0217

[46] Kogler, M., Chlyeh, Y., Krauss, R.: New ventilation concept with indirect ventilation through defrost air outlet. ATZ worldwide **109**(2), 25–28 (2007) https://doi.org/10.1007/BF03224912

[47] Yang, B., Huang, L.N., Ren, F.T.: Aerodynamic design and numerical simulation analysis of a passenger car's defrosting duct. In: Mechatronics and Applied Mechanics II. Applied Mechanics and Materials, vol. 300, pp. 1032–1035. Trans Tech Publications Ltd, ??? (2013). https://doi.org/10.4028/www.scientific.net/AMM.300-301.1032

[48] Sip, J., Lizal, F., Pokorny, J., Elcner, J., Jedelsky, J., Jicha, M.: Automotive cabin vent: Comparison of rans and les approaches with analytical-empirical equations and their validation with experiments using hot-wire anemometry. Building and Environment **233**, 110072 (2023) https://doi.org/10.1016/j.buildenv.2023.110072

[49] Choudhury, A.R., Anupindi, K.: Large-eddy simulation of a planar offset wall-jet with heat transfer: Characterization, turbulent kinetic energy and reynolds shear stress budgets. International Journal of Heat and Mass Transfer **191**, 122847 (2022) https://doi.org/10.1016/j.ijheatmasstransfer.2022.122847

[50] Uddin, N., Kee, P.T.W., Weigand, B.: Heat transfer by jet impingement: A review of heat transfer correlations and high-fidelity simulations. Applied Thermal Engineering **257**, 124258 (2024) https://doi.org/10.1016/j.applthermaleng.2024.124258

[51] Müller, S., Putin, P., Thole, C., Abdelhady, N.: Analyse der stabilität der strömung einer defrostanlage mit model order reduction [analysis of the stability of the flow in a defrosting system using model order reduction]. In: NAFEMS20 DACH Virtuelle Konferenz: Fachkonferenz Für Berechnung & Simulation Im Engineering: Conference Proceedings. NAFEMS Deutschland, ??? (2020)

[52] Pope., S.B.: Turbulent Flows. Cambridge University Press, ??? (2000)

[53] Deo, R.C., Mi, J., Nathan, G.J.: The influence of nozzle aspect ratio on plane jets. Experimental Thermal

and Fluid Science **31**(8), 825–838 (2007) https://doi.org/10.1016/j.expthermflusci.2006.08.009

[54] Deo, R.C., Nathan, G.J., Mi, J.: Comparison of turbulent jets issuing from rectangular nozzles with and without sidewalls. Experimental Thermal and Fluid Science **32**(2), 596–606 (2007) https://doi.org/10.1016/j.expthermflusci.2007.06.009

[55] LaVision: FlowMaster Product Manual. (2021). LaVision

[56] Wieneke, B.: Piv uncertainty quantification from correlation statistics. Measurement Science and Technology **26**(7), 074002 (2015) https://doi.org/10.1088/0957-0233/26/7/074002

[57] Sciacchitano, A., Wieneke, B.: Piv uncertainty propagation. Measurement Science and Technology **27**(8), 084006 (2016) https://doi.org/10.1088/0957-0233/27/8/084006

[58] Wieneke, B.: Piv uncertainty quantification and beyond. PhD thesis, TU Delft (2017)

[59] TSI: Portable Test Aerosol Generator Models 3073 Specifications. TSI

[60] Crowe, C.T.: Multiphase Flow Handbook, 1st edn. CRC Press, ??? (2005). https://doi.org/10.1201/9781420040470

[61] Topas GmbH: Di-Ethyl-Hexyl-Sebacate Excerpt from Material Safety Data Sheet of Manufacturer. Topas GmbH

[62] Launder, B.E., Rodi, W.: The turbulent wall jet measurements and modeling. Annual Review of Fluid Mechanics **15**(Volume 15, 1983), 429–459 (1983) https://doi.org/10.1146/annurev.fl.15.010183.002241

[63] Hoch, J., Jiji, L.M.: Two-dimensional turbulent offset jet-boundary interaction. Journal of Fluids Engineering **103**(1), 154–161 (1981) https://doi.org/10.1115/1.3240766 https://asmedigitalcollection.asme.org/fluidsengineering/article-pdf/103/1/154/5559578/154$_1$.*pdf*

[64] Squire, H.B.: Jet flow and its effects on aircraft: An analysis of experimental data on velocity and temperature distribution with a discussion of the effects of jets on drag and stability. Aircraft Engineering **22**(3), 62–67 (1950) https://doi.org/10.1108/eb031870 https://www.emerald.com/aeat/article-pdf/22/3/62/101403/eb031870.pdf

[65] Choudhary, H., Gupta, A., Bhatt, S., Prabhakaran, T., Singh, A.K., Karipot, A., Dixit, S.A.: Experimental investigation of the structure of plane turbulent wall jets. part 1. spectral analysis. Journal of Fluid Mechanics **988**, 42 (2024) https://doi.org/10.1017/jfm.2024.464

[66] Pelfrey, J.R.R., Liburdy, J.A.: Mean flow characteristics of a turbulent offset jet. Journal of Fluids Engineering **108**(1), 82–88 (1986) https://doi.org/10.1115/1.3242548 https://asmedigitalcollection.asme.org/fluidsengineering/article-pdf/108/1/82/5583781/82$_1$.*pdf*

[67] Song, H.-B., Yoon, S.-H., Lee, D.-H.: Flow and heat transfer characteristics of a two-dimensional oblique wall attaching offset jet. International Journal of Heat and Mass Transfer **43**(13), 2395–2404 (2000) https://doi.org/10.1016/S0017-9310(99)00312-9

[68] Akansu, Y.E., Sarioglu, M., Kuvvet, K., Yavuz, T.: Flow field and heat transfer characteristics in an oblique slot jet impinging on a flat plate. International Communications in Heat and Mass Transfer **35**(7), 873–880 (2008) https://doi.org/10.1016/j.icheatmasstransfer.2008.03.005

[69] Beltaos, S.: Oblique impingement of plane turbulent jets. Journal of the Hydraulics Division **102**(9), 1177–1192 (1976) https://doi.org/10.1061/JYCEAJ.0004605 https://ascelibrary.org/doi/pdf/10.1061/JYCEAJ.0004605

[70] Zhang, X., Yarusevych, S., Peterson, S.D.: Experimental investigation of flow development and coherent structures in normal and oblique impinging slot jets. Experiments in Fluids **60**(1), 11 (2018) https://doi.org/10.1007/s00348-018-2653-6

[71] O'Donovan, T.S., Murray, D.B.: Fluctuating fluid flow and heat transfer of an obliquely impinging air jet. International Journal of Heat and Mass Transfer **51**(25), 6169–6179 (2008) https://doi.org/10.1016/j.ijheatmasstransfer.2008.04.036

[72] Khan, F.R., Rielly, C.D., Brown, D.A.R.: Angle-resolved stereo-piv measurements close to a down-pumping pitched-blade turbine. Chemical Engineering Science **61**(9), 2799–2806 (2006) https://doi.org/10.1016/j.ces.2005.10.067 . Fluid Mixing VIII International Conference

[73] Ruiz, C.A., Hooff, T., Blocken, B., G. Heijst: Piv measurements and validation of rans solutions for plane turbulent impinging co-flowing and angled jets at moderate reynolds numbers. Flow, Turbulence and Combustion **114**(4), 1113–1147 (2025) https://doi.org/10.1007/s10494-025-00650-x

[74] Zuckerman, N., Lior, N.: Jet impingement heat transfer: Physics, correlations, and numerical modeling. Advances in Heat Transfer, vol. 39, pp. 565–631. Elsevier (2006). https://doi.org/10.1016/S0065-2717(06)39006-5 . https://www.sciencedirect.com/science/article/pii/S0065271706390065

[75] Yoon, S.-H., Kim, M.-K., Lee, D.-H.: Turbulent flow and heat transfer characteristics of a two-dimensional oblique plate impinging jet. KSME International Journal **11**(4), 476–483 (1997) https://doi.org/10.1007/BF02945086

[76] Neuendorf, R., Wygnanski, I.: On a turbulent wall jet flowing over a circular cylinder. Journal of Fluid Mechanics **381**, 1–25 (1999) https://doi.org/10.1017/S0022112098003668

[77] Yoon, S.-H., Kim, K.-C., Kim, D.-S., Chung, M.-K.: Comparative study of a turbulent wall-attaching offset jet and a plane wall jet. KSME Journal **7**(2), 101–112 (1993) https://doi.org/10.1007/BF02954360

[78] Georgiadis, N.J., Papamoschou, D.: Computational investigations of high speed dual stream jets. In: 9th AIAA/CEAS Aeroacoustics Conference and Exhibit (2003). https://api.semanticscholar.org/CorpusID:46657886

[79] GEORGE, W.K., ABRAHAMSSON, H., ERIKSSON, J., KARLSSON, R.I., M., L.L., WOSNIK: A similarity theory for the turbulent plane wall jet without external stream. Journal of Fluid Mechanics **425**, 367–411 (2000) https://doi.org/10.1017/S002211200000224X

[80] Barenblatt, G.I., Chorin, A.J., Prostokishin, V.M.: The turbulent wall jet: A triple-layered structure and incomplete similarity. Proceedings of the National Academy of Sciences **102**(25), 8850–8853 (2005) https://doi.org/10.1073/pnas.0503186102 https://www.pnas.org/doi/pdf/10.1073/pnas.0503186102

[81] Yang, L., Huang, H., Chen, M., Zhou, X., Jiang, P.: Entrainment mechanism in a turbulent offset jet. Ocean Engineering **342**, 122907 (2025) https://doi.org/10.1016/j.oceaneng.2025.122907

[82] ASHRAE Corporate Author: ASHRAE Handbook – 2008 HVAC Systems and Equipment (I-P Edition). American Society of Heating, Refrigerating and Air-Conditioning Engineers, Atlanta, GA (2008)

[83] Berkooz, G., Holmes, P., Lumley, J.L.: The proper orthogonal decomposition in the analysis of turbulent flows. Annual Review of Fluid Mechanics **25**(Volume 25, 1993), 539–575 (1993) https://doi.org/10.1146/annurev.fl.25.010193.002543

[84] Sirovich, L.: Turbulence and the dynamics of coherent structures. i. coherent structures. Quarterly of Applied Mathematics **45**, 561–571 (1987) https://doi.org/10.1090/qam/910462

[85] Welch, P.: The use of fast fourier transform for the estimation of power spectra: A method based on time averaging over short, modified periodograms. IEEE Transactions on Audio and Electroacoustics **15**(2), 70–73 (1967) https://doi.org/10.1109/TAU.1967.1161901

[86] Mood, A.M.: Introduction to the Theory of Statistics. Introduction to the theory of statistics., pp. –433433. McGraw-Hill, New York, NY, US (1950)

List of Figures

1 Automotive windshield defrosting components and Coandă effect. . . . 2
2 Pseudo-2D defrost testrig. . . . 6
3 Test rig parameters, pressure tap locations on windshield and PIV ROIs. . . . 7
4 Schematic representation of the fundamental flow topology and terminology. . . . 10
5 Primary jet state map and hysteresis. . . . 12
6 Instantaneous velocity magnitude displaying hysteresis in the primary jet behavior due to the Coandă effect. . . . 13
7 Pressure coefficient distribution on windshield surface for windshield-attached states. . . . 13
8 Normalized time-averaged velocity magnitude and turbulent kinetic energy contours for windshield-attached states. . . . 15
9 Normalized time-averaged velocity magnitude and turbulent kinetic energy contours for dashboard-attached states. . . . 18
10 Normalized maximum velocity variation. . . . 19
11 Normalized outer half-width for dashboard-attached states. . . . 20
12 Statistical analysis of random state switching. . . . 22
13 **(a)** Normalized temporal coefficients of the first two dominant POD modes of random state-switching with $\beta = 45°$ and $L_s = 32\,\text{mm}$ (1: switching mode, 2: relaxation mode).**(b)** Corresponding eigenfunctions. . . . 23
A1 Flow topology of dashboard-attached states db-A and db-B. . . . 25
B1 Normalized time-averaged velocity magnitude and turbulent kinetic energy fields for windshield-attached states with increased primary duct angle. . . . 28
C1 Normalized first- and second-order velocity field statistics in the outer layer of windshield-attached states with $\beta = 45°$. . . . 29
C2 Normalized first- and second-order velocity field statistics in the outer layer of dashboard-attached states with $\beta = 45°$. . . . 30
C3 Normalized first- and second-order velocity field statistics in the outer layer of windshield-attached states with $\beta = 61.9°$. . . . 31
C4 Normalized first- and second-order velocity field statistics in the outer layer of windshield-attached states with $\beta = 80.6°$. . . . 32
D1 Normalized outer and inner half-width for windshield-attached states. . . . 33

List of Tables

1 Overview of test rig parameters. . . . 5
2 Jet configurations with changing primary duct angle. . . . 7
3 Overview of PIV imaging and acquisition setup. . . . 9
4 Stagnation point location and eccentricity. . . . 14
5 Exponents of the power-law regression to the centerline velocity decay for windshield-attached states. . . . 14
6 Exponents of the power-law regression to the centerline velocity decay and outer half-width growth for dashboard attached states. . . . 19